AGU PUBLICATIONS

JGR

Journal of Geophysical Research: Solid Earth

RESEARCH ARTICLE
10.1002/2014JB011824

Key Points:
- We used a massive and varied data set to constrain radially anisotropic mantle structure
- We include crustal thickness perturbations as model parameters
- We observe faster SV velocity along subduction slabs in the transition zone

Supporting Information:
- Table S1 and Figures S1–S4

Correspondence to:
S.-J. Chang,
sjchang@kangwon.ac.kr

Citation:
Chang, S.-J., A. M. G. Ferreira, J. Ritsema, H. J. van Heijst, and J. H. Woodhouse (2015), Joint inversion for global isotropic and radially anisotropic mantle structure including crustal thickness perturbations, *J. Geophys. Res. Solid Earth*, *120*, 4278–4300, doi:10.1002/2014JB011824.

Received 10 DEC 2014
Accepted 11 MAY 2015
Accepted article online 15 MAY 2015
Published online 5 JUN 2015

Joint inversion for global isotropic and radially anisotropic mantle structure including crustal thickness perturbations

Sung-Joon Chang[1,2], Ana M. G. Ferreira[1,3,4], Jeroen Ritsema[5], Hendrik J. van Heijst[6], and John H. Woodhouse[7]

[1]School of Environmental Sciences, University of East Anglia, Norwich, UK, [2]Now at Division of Geology and Geophysics, Kangwon National University, Chuncheon, South Korea, [3]Now at Department of Earth Sciences, University College London, London, UK, [4]CEris, ICIST, Instituto Superior Tecnico, Universidade de Lisboa, Lisboa, Portugal, [5]Department of Earth and Environmental Sciences, University of Michigan, Ann Arbor, Michigan, USA, [6]Shell International Exploration and Production, Aberdeen, UK, [7]Department of Earth Sciences, University of Oxford, Oxford, UK

Abstract We present a new global whole-mantle model of isotropic and radially anisotropic *S* velocity structure (SGLOBE-rani) based on ~43,000,000 surface wave and ~420,000 body wave travel time measurements, which is expanded in spherical harmonic basis functions up to degree 35. We incorporate crustal thickness perturbations as model parameters in the inversions to properly consider crustal effects and suppress the leakage of crustal structure into mantle structure. This is possible since we utilize short-period group-velocity data with a period range down to 16 s, which are strongly sensitive to the crust. The isotropic *S* velocity model shares common features with previous global *S* velocity models and shows excellent consistency with several high-resolution upper mantle models. Our anisotropic model also agrees well with previous regional studies. Anomalous features in our anisotropic model are faster *SV* velocity anomalies along subduction zones at transition zone depths and faster *SH* velocity beneath slabs in the lower mantle. The derived crustal thickness perturbations also bring potentially important information about the crustal thickness beneath oceanic crusts, which has been difficult to constrain due to poor access compared with continental crusts.

1. Introduction

Since its identification in the 1960s [e.g., *Anderson*, 1961, 1965; *Aki and Kaminuma*, 1963; *Hess*, 1964; *McEvilly*, 1964], seismic anisotropy has been mapped in the upper mantle, the transition zone, the lowermost mantle, and the inner core (see, e.g., a recent review by *Chang et al*. [2014]). Seismic anisotropy provides invaluable information on mantle convection, since it is primarily caused by the alignment of intrinsically anisotropic minerals due to large-scale deformation. Seismic anisotropy can be a key proxy to infer the trajectories of mantle flow.

The simplest type of anisotropy is the so-called radial anisotropy (or transverse isotropy), which can potentially help distinguishing between horizontal and vertical mantle flow. Azimuthal anisotropy can provide constraints on the direction of horizontal mantle flow. Since different minerals have different slip directions that depend on temperature, pressure, and water content [e.g., *Jung and Karato*, 2001; *Karato et al*., 2008], the interpretation of observations of seismic anisotropy relies on experimental results from mineral physics.

Preliminary Reference Earth Model (PREM) [*Dziewoński and Anderson*, 1981], one of the most widely used 1-D reference models, incorporates radial anisotropy from the Moho (24.4 km depth) to the 220 km discontinuity. It is mainly constrained by joint analysis of Rayleigh and Love wave data. *Montagner and Anderson* [1989] and *Montagner and Kennett* [1996] modified PREM using additional normal-mode and travel time data, respectively. Moreover, *Beghein et al.* [2006] also modified PREM using normal-mode data in a wide frequency range. Fully 3-D radially anisotropic models for both the upper and whole mantle have been developed since the 1980s [e.g., *Nataf et al*., 1984, 1986; *Montagner and Tanimoto*, 1991; *Debayle and Kennett*, 2000; *Shapiro and Ritzwoller*, 2002; *Gung et al*., 2003; *Beghein and Trampert*, 2003, 2004; *Panning and Romanowicz*, 2004, 2006; *Kustowski et al*., 2008; *Nettles and Dziewoński*, 2008; *Visser et al*., 2008; *Ferreira et al*., 2010; *Panning et al*., 2010; *Lekić and Romanowicz*, 2011; *French et al*., 2013; *Auer et al*., 2014;

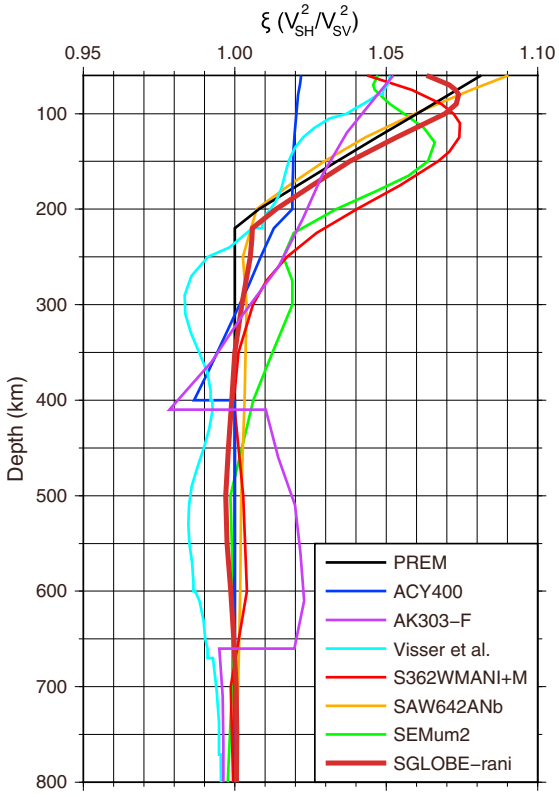

Figure 1. Comparison of 1-D radially anisotropic models from PREM [*Dziewoński and Anderson*, 1981], ACY400 [*Montagner and Anderson*, 1989], and AK303-F [*Montagner and Kennett*, 1996] with average 1-D profiles from 3-D anisotropic models from S362WMANI + M [*Moulik and Ekström*, 2014], *Visser et al.*'s [2008] model, SAW642ANb [*Panning et al.*, 2010], SEMum2 [*French et al.*, 2013], and the SGLOBE-rani model obtained in this study.

Moulik and Ekström, 2014] with increasing resolution. Initially, only fundamental-mode surface wave data were used to build the models [e.g., *Nataf et al.*, 1984, 1986; *Montagner and Tanimoto*, 1991; *Shapiro and Ritzwoller*, 2002]. Higher-mode surface waves have been incorporated since the early 2000s by, e.g., *Debayle and Kennett* [2000], *Gung et al.* [2003], *Beghein et al.* [2006], and *Visser et al.* [2008]. Travel time data (or body waveforms) were also used by *Panning and Romanowicz* [2006], *Kustowski et al.* [2008], *Panning et al.* [2010], *Auer et al.* [2014], and *Moulik and Ekström* [2014] to resolve radial anisotropy in the lower mantle. Since surface wave and body wave data have complementary depth sensitivities, it is useful to combine them in whole-mantle inversions to optimize the depth resolution throughout the whole mantle (see, e.g., resolution tests in *Chang et al.* [2014]). Discontinuity perturbations have also been included in inversions for radial anisotropy to account for trade-offs between discontinuities and isotropic and anisotropic anomalies [e.g., *Shapiro and Ritzwoller*, 2002; *Kustowski et al.*, 2008; *Visser et al.*, 2008; *Moulik and Ekström*, 2014].

In contrast to global isotropic shear velocity structure, we have not reached yet a consensus on the large-scale pattern of radial anisotropy in the Earth's mantle. Even 1-D models of radial anisotropy show substantial differences, particularly below the lithosphere (~250–400 km depth) and in the transition zone (~410–660 km) (Figure 1). Model disagreements highlight the subtle effects of radial anisotropy on seismic waveforms, which cannot be easily separated from the effects of isotropic structure.

Furthermore, the crust has a significant effect even on long-period surface waves [e.g., *Bozdağ and Trampert*, 2008]. To account for the effects of the crust, crustal corrections are usually applied to the data based on an a priori crustal model, whereby the predicted effects of crustal structure on seismic measurements are theoretically calculated and subtracted from the data. *Ferreira et al.* [2010] showed that the effects of crustal corrections on data misfits can be as large as those due to lateral variations in radial anisotropy. Waveform tomography might suffer from these issues even more severely due to highly nonlinear crustal effects [e.g., *Kustowski et al.*, 2007; *Marone and Romanowicz*, 2007; *Lekić et al.*, 2010].

Chang et al. [2014] reviewed these issues and developed a preliminary global *S* velocity radially anisotropic model based on the data set used to construct the mantle model S40RTS [*Ritsema et al.*, 2011], as well as Love wave dispersion measurements from the same authors. In this study, we use a much larger data set to better constrain radial anisotropy in the whole mantle. To reduce the effects of the crust on the mapping of radial anisotropy in the mantle, we use short-period group-velocity dispersion measurements to invert for crustal thickness. Group-velocity data have been used in the construction of global radially anisotropic models in a few studies. *Shapiro and Ritzwoller* [2002] used a Monte Carlo approach to constrain radially anisotropic and isotropic structures in the upper mantle as well as Moho depth using group-velocity data, but the allowed range of Moho depth is only 5 km from CRUST5.1

[*Mooney et al.*, 1998]. *Lekić and Romanowicz* [2011] and *French et al.* [2013] used group-velocity data to build "an equivalent average crustal model," which they used to perform crustal corrections on waveforms. However, they used data with periods longer than 25 s, which may not provide sufficient resolution to constrain crustal structure globally.

In this study we do not impose any preset range for crustal thickness variations, allowing the model parameters of crustal thickness to freely change, and we use group-velocity data with a period range down to 16 s. We discuss the methodology and data sets used in this study in sections 2 and 3. In section 4, we discuss the results from our anisotropic inversions, including comparisons with previous global studies and high-resolution regional studies. In sections 5 and 6, we present resolution tests and examine the data misfit variations due to isotropic, anisotropic, and crustal thickness model parameters.

2. Methodology

2.1. Theoretical Background

A radially anisotropic medium can be described by hexagonal symmetry with a vertical axis of symmetry, density, and the five independent elastic coefficients, A, C, F, L, and N [*Love*, 1927], called Love coefficients:

$$A = \rho V_{PH}^2 \tag{1}$$

$$C = \rho V_{PV}^2 \tag{2}$$

$$L = \rho V_{SV}^2 \tag{3}$$

$$N = \rho V_{SH}^2 \tag{4}$$

$$F = \frac{\eta}{A - 2L}, \tag{5}$$

where ρ is the density and V_{PH} and V_{PV} are the horizontally and vertically polarized P wave velocities, respectively. V_{SH} and V_{SV} are the horizontally and vertically polarized S wave velocities, respectively, and η is a parameter related to velocities at intermediate angle. In this study isotropic and radially anisotropic S velocity structures are parameterized as in *Ferreira et al.* [2010]:

$$v_S^2 = \frac{1}{2}\left(V_{SV}^2 + V_{SH}^2\right) \text{ and } \zeta_S = \frac{V_{SH}^2 - V_{SV}^2}{2v_S^2}. \tag{6}$$

While there is some subjectivity in the choice of model parameterization [e.g., *Lévêque and Cara*, 1985], using the Love parameters is particularly useful for a more direct comparison with elastic parameters obtained in mineral physics experiments.

In order to keep the problem tractable, we scale perturbations of V_P and density to perturbations of V_S using the scaling relations $\frac{\delta V_P}{V_P} = 0.5\frac{\delta V_S}{V_S}$ [*Robertson and Woodhouse*, 1995] and $\frac{\delta \rho}{\rho} = 0.4\frac{\delta V_S}{V_S}$ [*Anderson et al.*, 1968], respectively. These scaling factors are only approximate, and there are studies [e.g., *Ishii and Tromp*, 1999; *Resovsky and Trampert*, 2003] that found little correlation between density and velocity anomalies in the lowermost mantle. Nevertheless, the body and surface wave data typically used in tomography studies are much more sensitive to shear wave speed than to compressional velocity and density. Hence, these scaling relations are still widely used in global tomography to reduce the number of parameters in the inversions.

The three physical model parameters in this study are perturbations in isotropic S velocity (v_S), S radial anisotropy (ζ_S), and crustal thickness (d). We write the inverse problem as

$$\delta e = \int_{\text{CMB}}^{a} \left\{K_{v_S}\delta v_S + K_{\zeta_S}\delta\zeta_S + K_d\delta d\right\} dr, \tag{7}$$

where δe is the difference between the data and theoretical calculations for a given reference model; r is the Earth's radius parameter; a is the Earth's radius; and δv_S, $\delta\zeta_S$, and δd are the perturbations of isotropic S velocity, S radial anisotropy, and crustal thickness. The kernels, K_{v_S}, K_{ζ_S}, and K_d, with respect to isotropic S velocity, S anisotropy, and crustal thickness relate the observations to the Earth's structure parameters, δv_S, $\delta\zeta_S$, and δd and will be discussed in more detail in the next section.

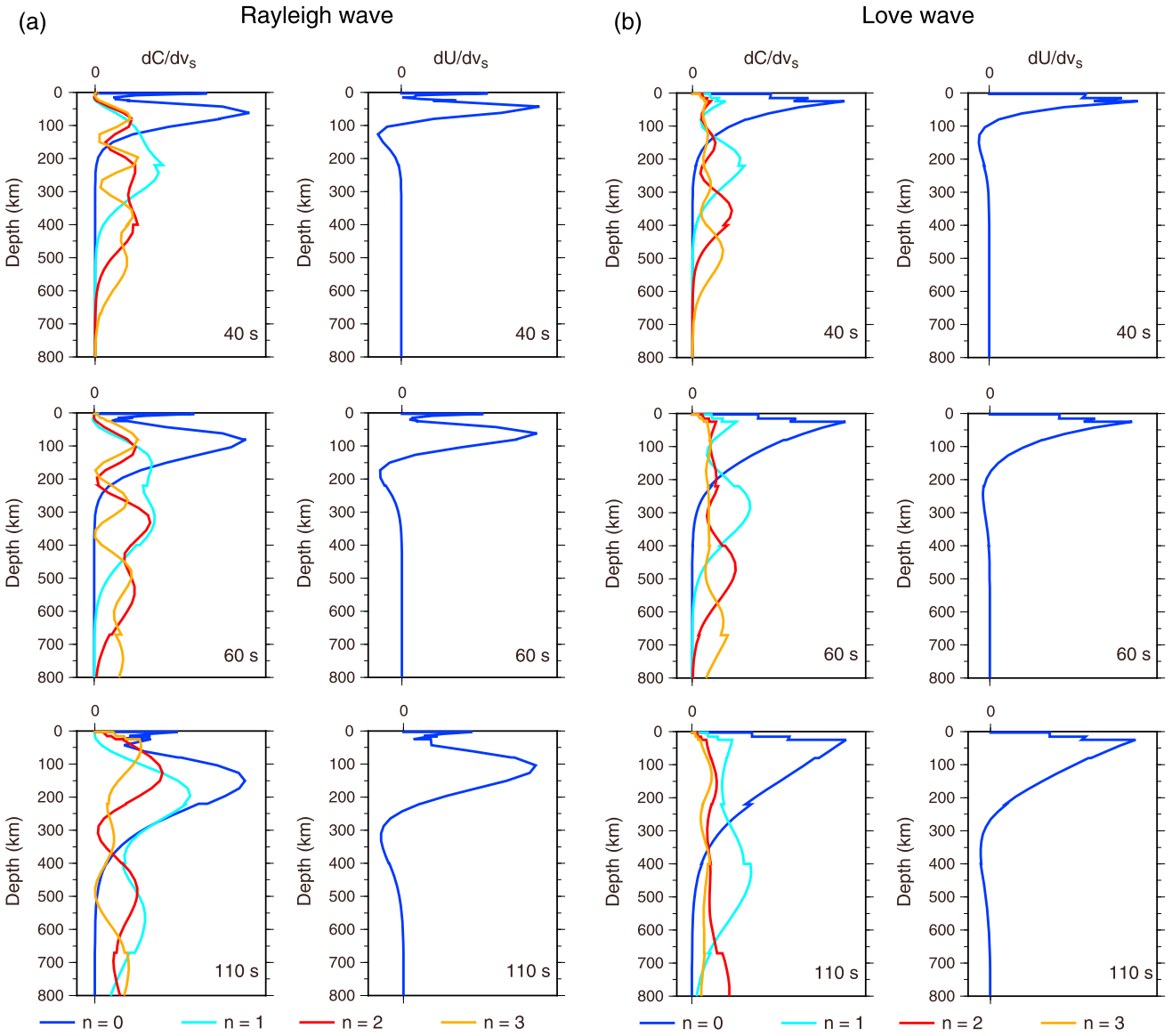

Figure 2. (a) Normalized Rayleigh wave phase-velocity kernels with respect to isotropic shear wave velocity $\left(\frac{dC}{dv_S}\right)$ at periods of 40, 60, and 110 s from top to bottom on the left-hand side. The kernels for fundamental mode are depicted in blue, and the kernels of overtones up to number 3 are indicated in cyan, red, and orange colors. Group-velocity kernels with respect to isotropic shear wave velocity $\left(\frac{dU}{dv_S}\right)$ are shown on the right-hand side. The details are the same as in the left column. (b) Same as in Figure 2a but for Love waves. The 1-D reference model PREM is used to compute the kernels.

2.2. Sensitivity Kernels

Sensitivity kernels for phase velocities are calculated using the great circle approximation and the formulation of *Takeuchi and Saito* [1972]. Sensitivity kernels for group velocities are constructed from the partial derivatives of phase velocities following *Rodi et al.* [1975].

Several examples of the sensitivity kernels of fundamental and higher-mode Rayleigh and Love waves with respect to *S* wave isotropic and anisotropic structures for PREM are shown in Figures 2 and 3, respectively. The sensitivity kernels have several important characteristics. As wave period increases, the peak sensitivity is at larger depths. With increasing overtone number, the number of peaks in the kernels increases. Overtones are more sensitive to structure below ~300 km depth than fundamental modes. The sensitivity kernels for group velocity have maxima at shallower depths than the phase-velocity kernels for the same wave period. This indicates that group-velocity data are more sensitive to shallower structure

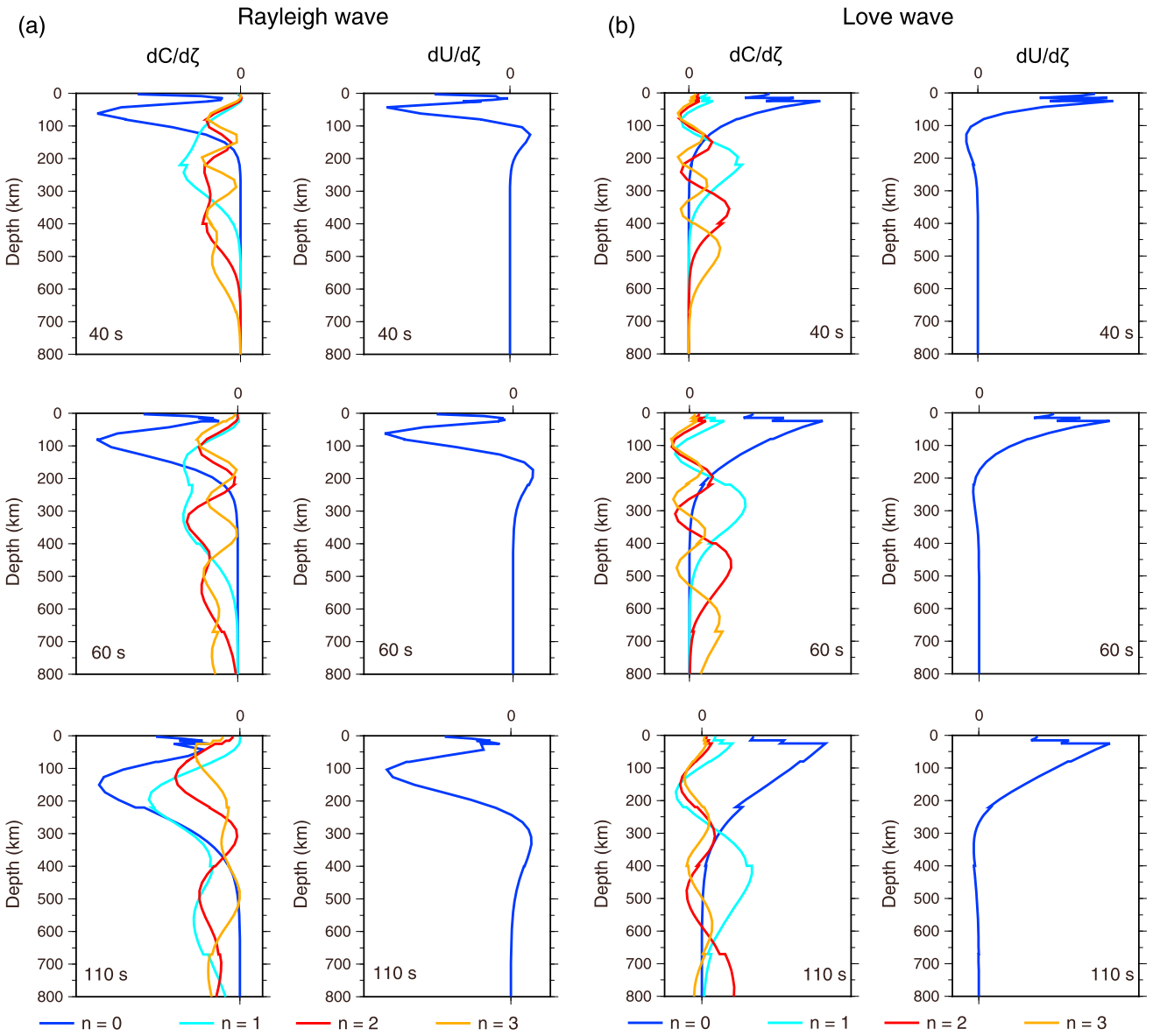

Figure 3. Same as in Figure 2 but for kernels with respect to radial anisotropy (ζ).

[e.g., *Lebedev et al.*, 2013]. Finally, the sensitivity kernels of Rayleigh waves and Love waves with respect to anisotropy have opposite signs.

Body wave travel time sensitivity kernels are calculated using the formalism of *Woodhouse* [1981] and *Woodhouse and Girnius* [1982]. Several examples of sensitivity kernels of *S*, *Sdiff*, and *SKS* phases with respect to *S* wave isotropic and anisotropic structures are shown in Figures 4 and 5, respectively. The sensitivity kernels with respect to δv_S are always negative, since positive velocity perturbations along the paths always reduce the travel times. The sign of the sensitivity kernels of *S* phases with respect to $\delta\zeta_S$ depends on the traveling angle. The *SKS* sensitivity kernels with respect to $\delta\zeta_S$ are always positive, because *SKS* phases are always sensitive to the *SV* wave speed. Thus, positive anisotropic perturbations ($V_{SH} > V_{SV}$) increase *SKS* travel times.

Sensitivity kernels with respect to crustal thickness are calculated using the formulation of *Woodhouse and Dahlen* [1978] for the phase-velocity data and by numerical differentiation for the group velocities and travel times.

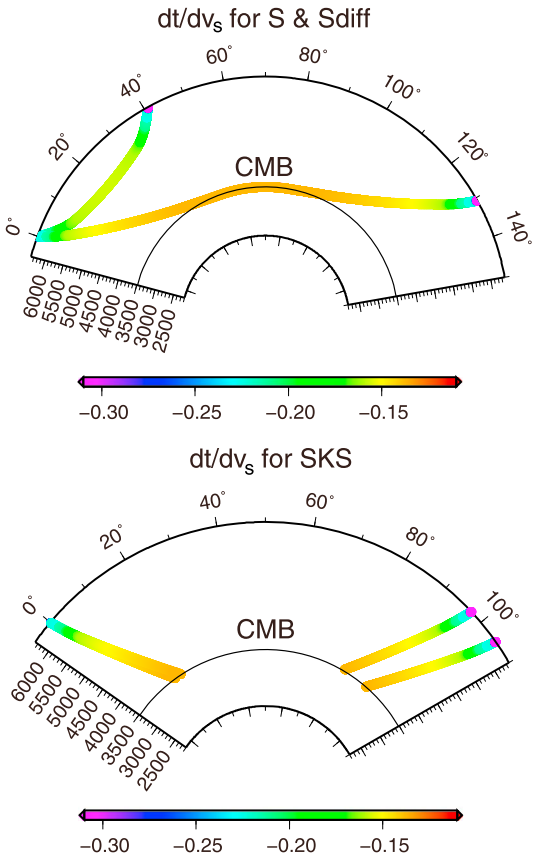

Figure 4. Sensitivity kernels of body wave travel times with respect to isotropic shear wave velocity (v_S). (top) Sensitivity kernels for *S* and *Sdiff* phases. (bottom) Sensitivity kernel for *SKS* phase.

We take into account physical dispersion effects due to attenuation by following the same approach as in PREM [*Dziewoński and Anderson*, 1981]. Specifically, attenuation is implemented using PREM's five-layer attenuation model with constant-*Q* logarithmic dispersion laws and a reference frequency of 1 Hz. While it is known that the effect of attenuation on inversions of body waves and normal modes can be large, it is difficult to constrain it robustly in global tomographic inversions [e.g., *Montagner and Kennett*, 1996].

2.3. Crustal Effects

We account for the effects of the crust on the data in two steps. First, we apply crustal corrections to all the data used in the inversions using the global crustal model CRUST2.0 [*Bassin et al.*, 2000]. We calculate crustal corrections for the surface wave data following the same approach as that of *Ferreira et al.* [2010]. We superimpose the CRUST2.0 model on PREM and calculate the local eigenfrequencies of the surface wave-equivalent modes in the 2°×2° grid of CRUST2.0. The path-integrated phase or group-velocity perturbation is then subtracted from each individual measurement. It is much easier to correct the effect of crustal structure on surface wave dispersion data than on waveforms, since local eigenfrequencies can be calculated exactly using normal-mode theory [e.g., *Takeuchi and Saito*, 1972] taking nonlinear effects fully into account. On the other hand, the crustal corrections of the body wave travel times are obtained from cross correlations of arrival time measurements on normal-mode summation synthetic seismograms. Different crustal models are used beneath the source and the receiver according to the model CRUST2.0 [*Ritsema et al.*, 2009].

Second, we estimate crustal thickness perturbations from CRUST2.0 in our joint inversions. Given that the data are corrected for CRUST2.0, we use crustal-thickness sensitivity kernels computed for PREM, which is a computationally efficient strategy. Nonlinear crustal effects are much alleviated by the crustal corrections, so the use of 1-D sensitivity kernels for crustal thickness, mantle velocity, and mantle anisotropy is reasonable. Moreover, *Kustowski et al.* [2007] showed that while considering lateral variations in the sensitivity kernels may somewhat affect the amplitudes of the retrieved anomalies in the inversions, the effect on the pattern of heterogeneity is minor. As shown later in section 5, resolution tests for crustal thickness show that perturbations of ~30 km beneath Tibet are recovered well with our strategy (Figure 17).

2.4. Parameterization and Inversion Scheme

We use spherical harmonic basis functions expanded up to degree 35 to parameterize the horizontal variation in v_S, ζ_S, and d, corresponding to a minimum grid side length of ~600 km. A total of 21 depth spline functions parameterize variations in the radial direction (see, e.g., Figure 4 in *Ritsema et al.* [2004]).

We solve the inverse problem in equation (7) using a damped least squares inversion scheme, and we use the 1-D reference model PREM as the starting model. Following a similar approach to *Ferreira et al.* [2010], we build the inner-product matrix of the sensitivity kernels, which is inverted using an eigenvalue decomposition scheme. We invert for a total of 55,728 parameters: 1296 model coefficients for crustal thickness perturbations, 27,216 for isotropic variations, and 27,216 for anisotropic variations. In order to

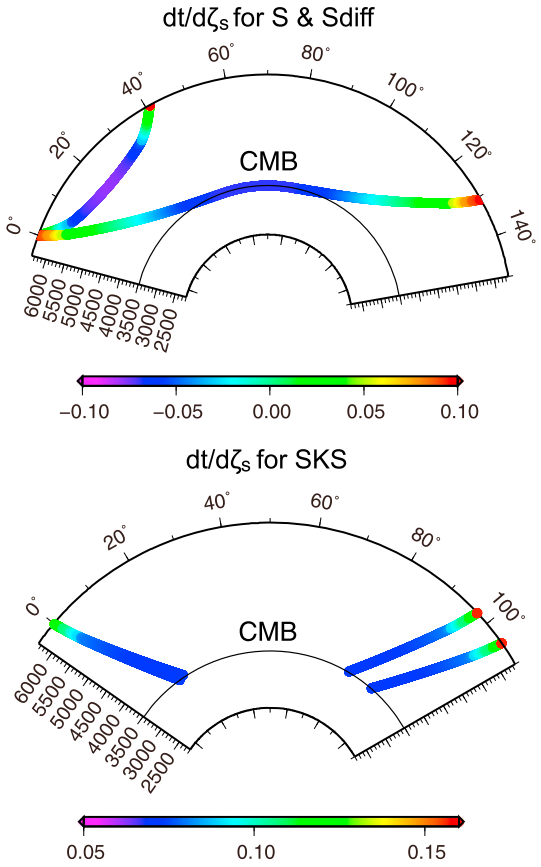

Figure 5. Sensitivity kernels of body wave travel times with respect to radial anisotropy (ζ). (top) Sensitivity kernels for *S* and *Sdiff* phases. (bottom) Sensitivity kernel for *SKS* phase.

stabilize the inversions, we apply norm damping for horizontal regularization; no explicit radial damping is imposed in the inversions. Since the resolving power of the data is weaker for anisotropy than for isotropic structure, it is necessary to apply stronger damping to the anisotropic parameters than to the isotropic parameters. By experimentation, we found that by applying ~1.3 times more damping to the anisotropic parameters than to the isotropic parameters helped suppress apparently artificial small-scale perturbations in the retrieved anisotropy models while keeping persistent large-scale structures.

We weigh each source-receiver path according to the number of similar paths within 1° from the station and from the event's location. This homogenizes the source-receiver path distribution in the inversions and optimizes the balance between the various data sets used.

3. Data

We use a total of ~43,000,000 surface wave measurements and ~420,000 travel time data in our study. We use the fundamental-mode phase-velocity dispersion measurements from *Ekström et al.* [1997] and *Ekström* [2011], which cover a period range of 35–300 s and 25–250 s, respectively. We also use higher-mode and fundamental-mode phase-velocity data from *van Heijst and Woodhouse* [1999], *Ritsema et al.* [2004], *Visser et al.* [2008], and *Ritsema et al.* [2011] for the period range of 35–375 s. The group-velocity measurements from *Ritzwoller and Levshin* [1998] with a period range of 16–150 s are particularly useful to constrain crustal structure. A summary of surface wave measurements for each mode used in this study is given in Table 1. Teleseismic body wave travel time data are obtained from *Ritsema et al.* [2011], with the number of travel time measurements for each phase used in this study being listed in Table 2.

We carried out extensive comparisons of the various data sets and checked whether they were consistent with each other before combining all the measurements. Moreover, we performed several inversion experiments using the various subsets of data to verify the compatibility of the images obtained. The availability of common measurements for some modes and paths in the various subsets of surface wave data was particularly useful to identify occasional outliers in the original data sets, which were not used in our inversions. Table S1 in the supporting information summarizes the outliers identified in this study.

4. Isotropic and Radially Anisotropic Model

Here we present our isotropic and radially anisotropic whole-mantle model SGLOBE-rani, including crustal thickness perturbations. As explained previously, the main differences from previous studies are that (1) we use a larger data set of body wave travel times and surface wave dispersion measurements including short-period group-velocity data and (2) we invert jointly for isotropic, anisotropic, and crustal thickness perturbations as model parameters. For the purpose of comparisons with other tomographic models, we convert the retrieved parameters to the Voigt average, $V^2_{\text{Voigt}} = \frac{2V^2_{SV}+V^2_{SH}}{3}$, and radial anisotropy, $\xi = \frac{N}{L} = \frac{V^2_{SH}}{V^2_{SV}}$, parameters.

Table 1. Number of Surface Wave Measurements Used in This Study[a]

	Spheroidal Mode		Toroidal Mode	
Data (Phase/Group)	Mode Number and Period Range	Number	Mode Number and Period Range	Number
Ekström et al. [1997] (*P*)	Fundamental mode (35~300 s)	276,812	Fundamental mode (35~300 s)	161,568
Ekström [2011] (*P*)	Fundamental mode (25~250 s)	2,548,680	Fundamental mode (25~250 s)	661,215
Ritsema et al. [2004] (*P*)	Fundamental mode (37.6~374 s)	2,693,926		
	first overtone (37.5~274 s)	223,672		
	second overtone (37.6~365 s)	193,919	Fundamental mode (37.6~375 s)	256,574
	third overtone (37.5~203 s)	169,908	first overtone (37.5~200 s)	64,861
	fourth overtone (37.5~78 s)	129,505	second overtone (37.5~114 s)	20,679
	fifth overtone (37.5~62 s)	68,282	third overtone (37.6~78 s)	9,438
	sixth overtone (88~132 s)	35		
Visser et al. [2008] (*P*)	Fundamental mode (35.1~175 s)	1,018,048	Fundamental mode (35.1~174 s)	722,864
	first overtone (35.1~173 s)	864,560	first overtone (35.1~177 s)	557,744
	second overtone (35~149 s)	786,855	second overtone (35~115 s)	412,152
	third overtone (35~88 s)	536,382	third overtone (35.1~79 s)	241,020
	fourth overtone (35.1~62 s)	324,848	fourth overtone (35.1~63 s)	120,520
	fifth overtone (35.1~56 s)	221,459	fifth overtone (35.1~56 s)	59,598
Ritzwoller and Levshin [1998] (*G*)	Fundamental mode (16~150 s)	1,083,328	Fundamental mode (16~100 s)	539,147
Ritsema et al. [2011] (*P*)	Fundamental mode (Vertical, 37.6~374 s)	13,202,786		
	Fundamental mode (Radial, 37.6~374 s)	3,717,227		
	first overtone (Vertical, 37.5~274 s)	991,490		
	first overtone (Radial, 37.5~274 s)	39,901	Fundamental mode (37.6~375 s)	5,244,236
	second overtone (Vertical, 37.6~365 s)	840,796	first overtone (37.5~382 s)	1,594,217
	second overtone (Radial, 37.6~365 s)	96,887	second overtone (37.5~324 s)	493,383
	third overtone (Vertical, 37.5~233 s)	723,823	third overtone (37.6~206 s)	230,714
	third overtone (Radial, 56~324 s)	171,253	fourth overtone (37.6~151 s)	104,108
	fourth overtone (Vertical, 37.5~130 s)	474,706	fifth overtone (37.5~56 s)	57,561
Sum		31,399,088		11,551,599

[a]"*P*" refers to phase-velocity measurements, while "*G*" refers to group-velocity measurements.

4.1. Isotropic Model

We compare our Voigt average isotropic *S* velocity model with previous whole-mantle and upper mantle *S* velocity models in Figure 6 (see enlarged figures of SGLOBE-rani in Figure S1 in the supporting information). S362WMANI + M [*Moulik and Ekström*, 2014], SAW642ANb [*Panning et al.*, 2010], S40RTS [*Ritsema et al.*, 2011], and SAVANI [*Auer et al.*, 2014] are whole-mantle *S* velocity models based on surface wave and body wave data, while SEMum2 [*French et al.*, 2013] and SL2013sv [*Schaeffer and Lebedev*, 2013] are upper mantle *S* velocity models. Shear velocity variations in the anisotropic models, S362WMANI + M, SAW642ANb, SAVANI, and SEMum2 are represented by the Voigt average $\left(V^2_{\text{Voigt}} = \frac{2V^2_{SV}+V^2_{SH}}{3}\right)$ variations.

Table 2. Phases and Corresponding Numbers of Body Wave Travel Time Data Used in This Study

Phase	Number	Component
S	172,738	Transverse
SS	114,270	Transverse
SSS	25,097	Transverse
ScS	8,517	Transverse
ScS2	13,590	Transverse
ScS3	8,025	Transverse
SKS	32,309	Radial
SKKS	8,839	Radial
sS	20,238	Transverse
sSS	9,770	Transverse
sSSS	2,763	Transverse
sScS	1,606	Transverse
sScS2	3,483	Transverse
sSKS	2,465	Radial
Sum	423,710	

The models have several common features: high-velocity anomalies beneath cratons at 100–150 km depth, low-velocity anomalies beneath ridges at 100–150 km depth, and high-velocity anomalies corresponding to subducting slabs in the transition zone and two Large Low Shear Velocity Provinces (LLSVPs) beneath Africa and the South Pacific in the lowermost mantle. However, our isotropic model along with a recent whole-mantle model, SAVANI, shows stronger perturbations at 100–150 km depth compared with other whole-mantle models, especially higher-velocity anomalies beneath cratons, which are more consistent with the upper mantle models. Furthermore, there are

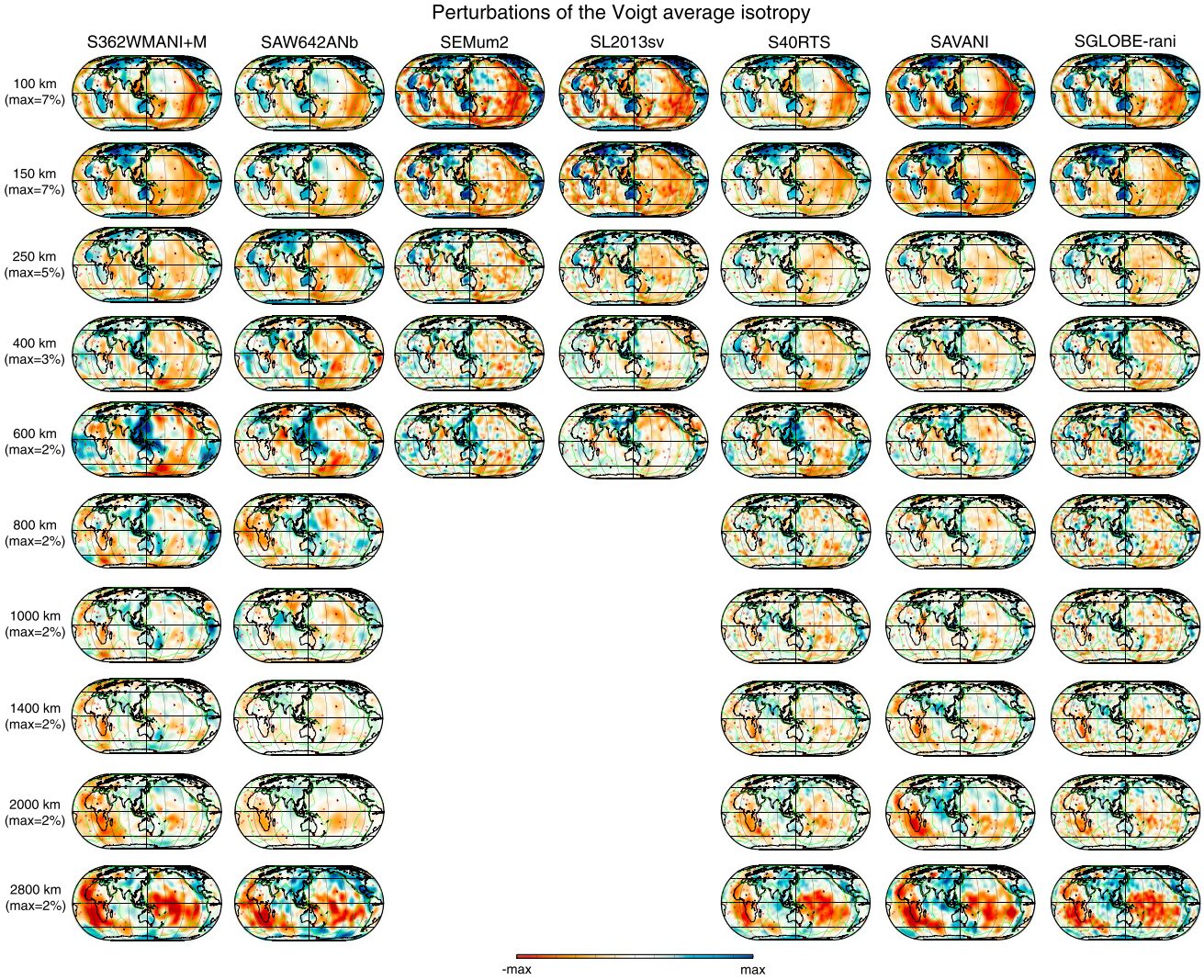

Figure 6. Comparison of the isotropic V_s structure (Voigt average, dV_{Voigt}/V_{Voigt}) in SGLOBE-rani with recent 3-D global isotropic shear wave velocity models, S362WMANI + M [*Moulik and Ekström*, 2014], SAW642ANb [*Panning et al.*, 2010], S40RTS [*Ritsema et al.*, 2011], SL2013sv [*Schaeffer and Lebedev*, 2013], and SEMum2 [*French et al.*, 2013]. Depth slices of perturbations of isotropic shear velocities from average values at 100, 150, 250, 400, 600, 800, 1000, 1400, 2000, and 2800 km are shown. The range of model amplitude variations is shown at the left of each row.

two small-scale low-velocity anomalies beneath Mongolia and Tibet at 100 km in SGLOBE-rani, which are also observed in the two upper mantle models but not in the other whole-mantle models. SAVANI also shows these two low-velocity anomalies but with different size and amplitude. High-velocity anomalies associated with subducting slabs at depths of ~400–600 km appear finely delineated as linear features in SGLOBE-rani, which are hardly observed or more patchy in the other whole-mantle models, but visible in the upper mantle models as well. Therefore, at least qualitatively, SGLOBE-rani seems to be more consistent with the two upper mantle models considered.

In Figure 7 (see enlarged figures of SGLOBE-rani in Figure S2 in the supporting information), we compare three cross sections from our Voigt average isotropic *S* model with the *S* velocity model S40RTS and the *P* velocity model GAP_P4 [*Fukao and Obayashi*, 2013]. Due to the use of a massive set of *P* wave travel time data, GAP_P4 resolves well subducting slabs; hence, the comparison of SGLOBE-rani with GAP_P4 is a useful means to assess the quality of our images, particularly for subduction zones.

Figure 7a shows that a broad lower mantle low-velocity anomaly beneath southern Africa, which has been previously referred to as the "African superplume," is observed in both *S* velocity models, splitting into two segments in the upper mantle. The split is more clearly separated in SGLOBE-rani, and the low-velocity

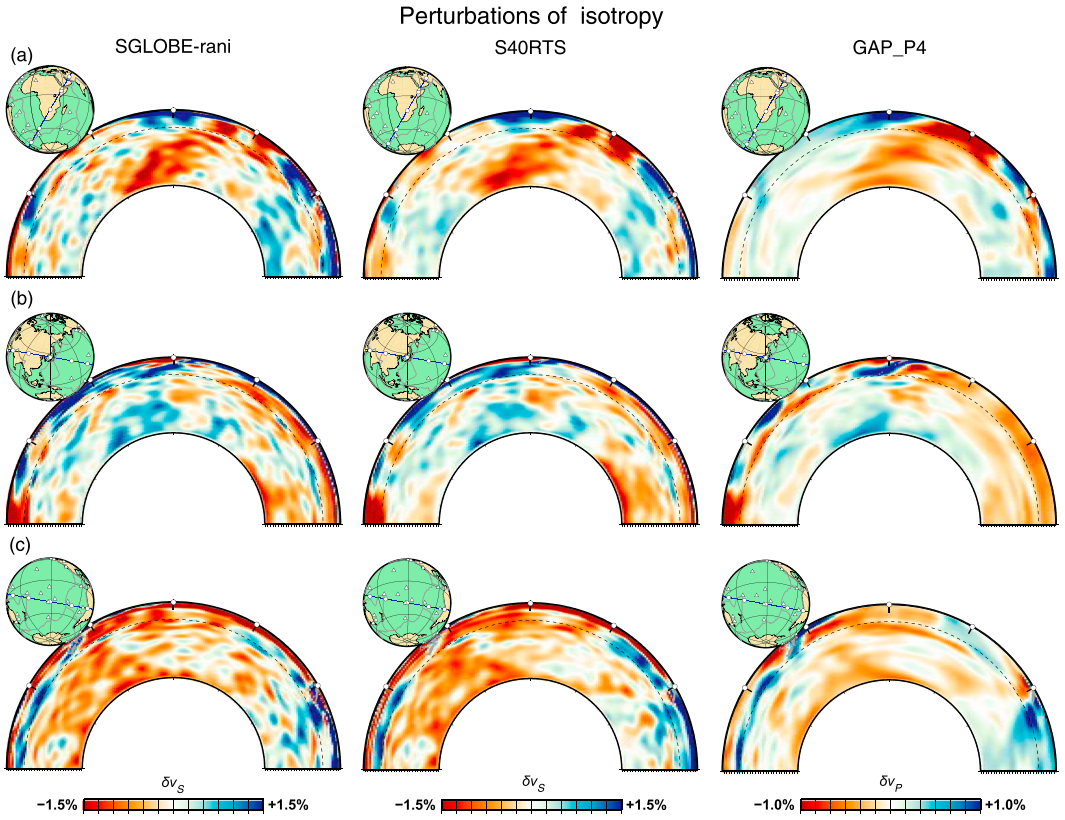

Figure 7. Depth cross sections throughout the whole mantle from the isotropic V_s structure (Voigt average, dV_{Voigt}/V_{Voigt}) in SGLOBE-rani, S40RTS [*Ritsema et al*., 2011], and GAP_P4 [*Fukao and Obayashi*, 2013]. Cross sections across (a) Africa, (b) East Asia, and (c) the South Pacific are shown. The dashed line corresponds to the 660 km discontinuity.

anomaly beneath Afar seems to be rooted to a different direction from the African superplume [*Debayle et al*., 2001; *Chang and van der Lee*, 2011], casting doubt on the argument that a single large mantle plume has caused volcanic activity in East Africa [*Nyblade*, 2011; *Hansen et al*., 2012]. GAP_P4 does not discern the two low-velocity anomalies in the upper mantle, but it seems to show the root of the Afar plume reaching the uppermost lower mantle with a different direction from that of the African superplume, as shown in SGLOBE-rani. Furthermore, subducting slabs beneath the Scotia Sea and Iran seem to appear clearly in SGLOBE-rani, reaching the mantle transition zone and the core-mantle boundary, respectively.

In Figure 7b, a high-velocity linear feature associated with the subducting Pacific plate beneath Japan is well observed in all three models. The morphology and thickness of the subducting slab in the *S* velocity models are comparable to those in the *P* velocity model, suggesting that both *S wave* speed models resolve subducting slabs well in this region.

In Figure 7c, SGLOBE-rani shows clearly a high-velocity anomaly associated with the Tonga slab, with an excellent match to the slab's deep seismicity (gray circles) and a similar slab geometry to that shown in GAP_P4. Moreover, in Figure 7c, SGLOBE-rani also shows a subducting slab (high-velocity anomaly) beneath the Andes, which is thicker than the Tonga slab and penetrating into the lower mantle. The slab in SGLOBE-rani has a similar geometry to that in the model GAP_P4. Therefore, SGLOBE-rani seems to image the structure of global subducting slabs similarly to the high-resolution *P* velocity model, GAP_P4.

4.2. Anisotropic Model

In Figure 8 (see enlarged figures of SGLOBE-rani in Figure S3 in the supporting information), we compare depth slices of perturbations ($\delta\xi$) in our radial anisotropy model with those from previous whole-mantle (S362WMANI + M, SAW642ANb, and SAVANI) and upper mantle (SEMum2) radially anisotropic models. These depth slices show perturbations from the mean values at each depth. We observe some similarities between the models, such as faster *SH* velocity anomalies beneath the Pacific at 150 km depth and faster

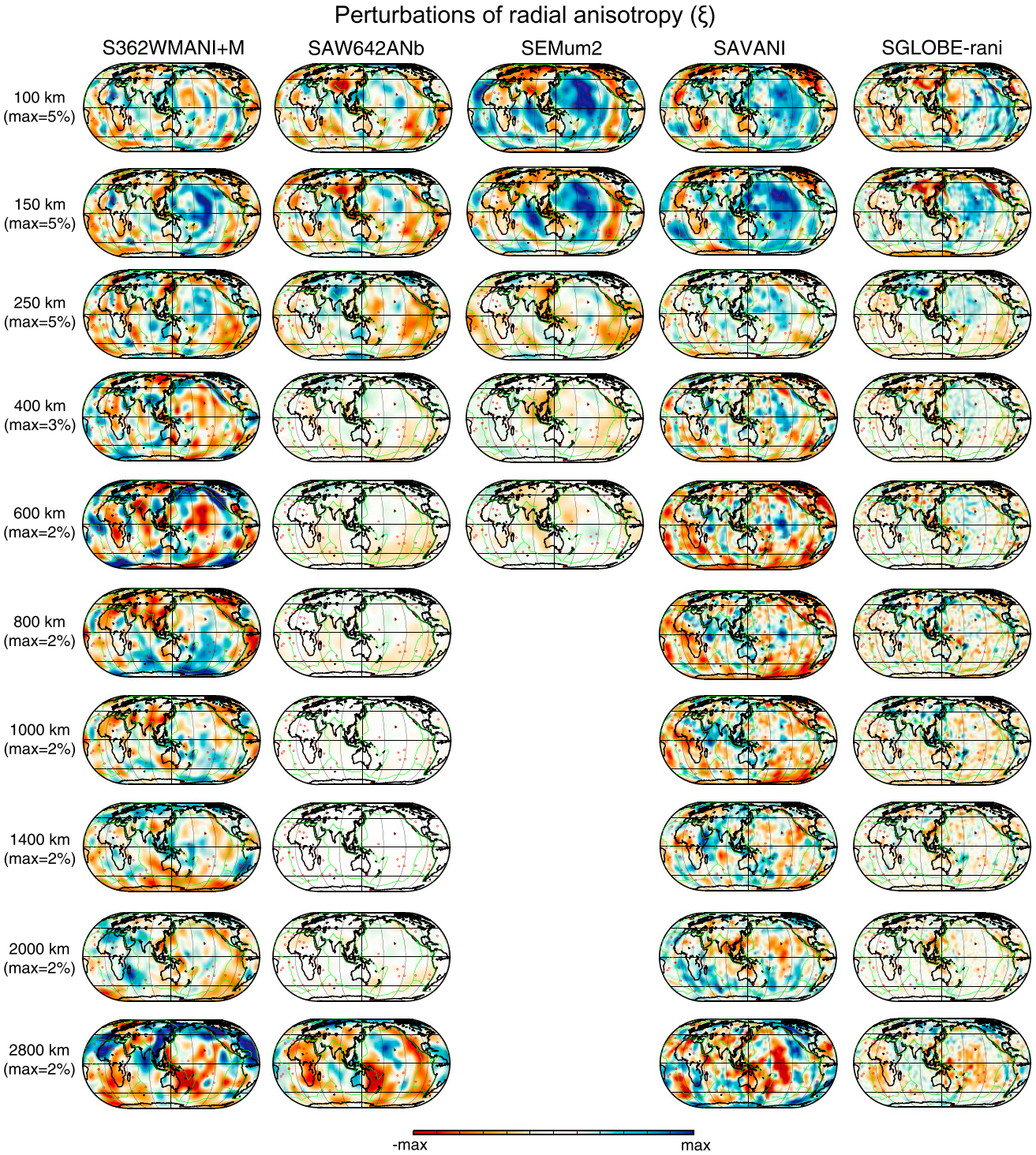

Figure 8. Comparison of the radially anisotropic structure in SGLOBE-rani with recent 3-D global radially anisotropic models S362WMANI + M [*Moulik and Ekström*, 2014], SAW642ANb [*Panning et al.*, 2010], and SEMum2 [*French et al.*, 2013]. Depth slices of perturbations of radial anisotropy $\left(\frac{d\xi}{\xi}\right)$ from average values at 100, 150, 250, 400, 600, 800, 1000, 1400, 2000, and 2800 km are shown. The range of model amplitude variations is shown at the left of each row.

SV velocity anomalies beneath the East Pacific Rise at 250 km depth. However, there are also quite substantial discrepancies between the models, much larger than for the isotropic models shown in Figure 6. For completeness, we also show depth slices of absolute radial anisotropy $\left(\xi = V_{SH}^2/V_{SV}^2\right)$ from all models in Figure 9 (see enlarged figures of SGLOBE-rani in Figure S4 in the supporting information).

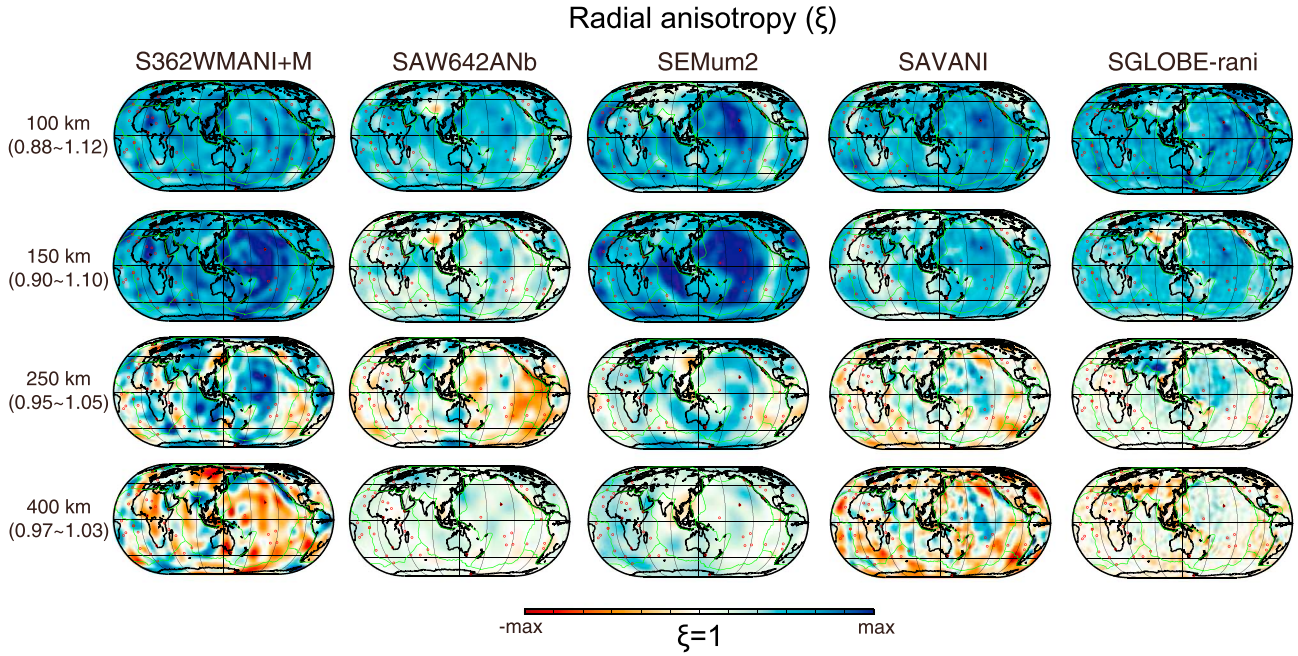

Figure 9. Same as in Figure 8 but for the absolute values of radial anisotropy $\left(\xi = \frac{V_{SH}^2}{V_{SV}^2}\right)$ at 100, 150, 250, and 400 km depths. The range of variations in ξ is shown at the left of each row.

In order to assess the various models in an independent way, we compare the models with results from regional studies of radial anisotropy, which are summarized in Figure 10. First, faster *SH* velocity anomalies at 150 km depth beneath the Pacific have been reported in several studies since the late 1980s [e.g., *Cara and Lévêque*, 1988; *Nishimura and Forsyth*, 1989; *Montagner and Tanimoto*, 1991; *Ekström and Dziewoński*, 1998; *Gung et al.*, 2003; *Nettles and Dziewoński*, 2008], which are observed in all the models shown in Figure 8. The same kind of feature is also observed in the asthenosphere beneath the Philippine Sea Plate by a recent study using broadband ocean bottom seismometers [*Takeo et al.*, 2013], which is also shown in all the models.

Second, *Gu et al.* [2005] reported that beneath the East Pacific Rise the faster axis of radial anisotropy changes from a vertical direction at ~200–300 km depth to a horizontal direction at ~100 km depth. This change in the polarity of radial anisotropy was interpreted as being due to a change in direction of mantle flow from vertical flow at ~200–300 km depth to horizontal asthenospheric flow directing plate motions at shallower depths. These features are observed in SGLOBE-rani but not in the models SAW642ANb and SEMum2 (Figures 8 and 9).

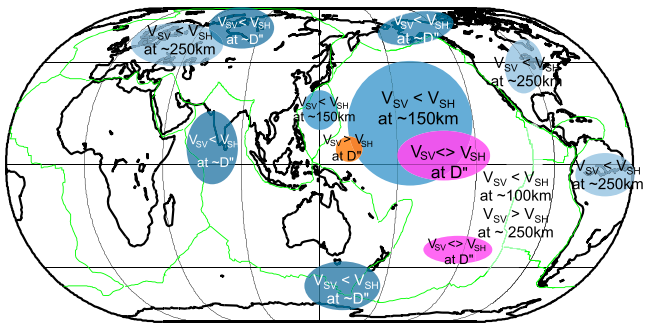

Figure 10. Summary of results from previous high-resolution regional studies of radial anisotropy. The blue color represents regions where *SH* velocity has been found faster than *SV* velocity, while the orange color means regions where *SV* velocity is faster than *SH* velocity. The purple color indicates regions where mixed anisotropy is observed (see main text for further details).

Third, it has been asserted that the lithosphere-asthenosphere boundary may be the locus of an abrupt change in radial anisotropy from frozen-in anisotropy associated with the past strain field in the lithosphere to anisotropy in the asthenosphere due to present mantle flow [*Silver*, 1996; *Montagner*, 1998]. *Gung et al.* [2003] reported that faster *SH* velocity is present at the bottom of continental and oceanic lithospheres, ~80–250 km depth beneath oceanic lithosphere and

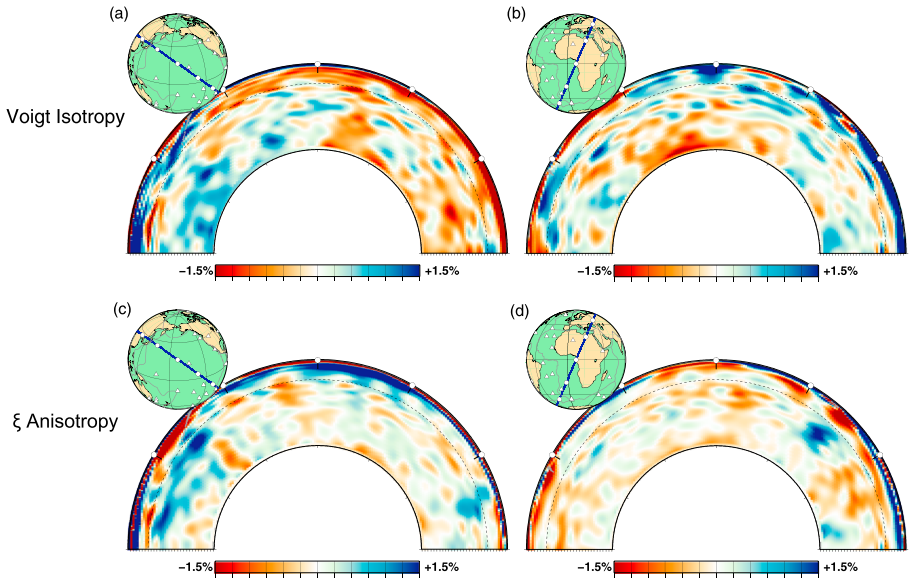

Figure 11. Depth cross sections throughout the whole mantle from the isotropic and radially anisotropic structures in SGLOBE-rani. (a and c) Isotropic and anisotropic cross sections across the Pacific are presented, respectively, (b and d) while isotropic and anisotropic cross sections across Africa are shown, respectively. The dashed line corresponds to the 660 km discontinuity, and the gray circles represent earthquakes.

~250–400 km beneath continental lithosphere. All the anisotropic models shown in Figures 8 and 9 seem to indicate this feature except for SEMum2; nevertheless, one should bear in mind that these models cannot resolve sharp discontinuities corresponding to abrupt changes in radial anisotropy.

Finally, there are ample reports on radial anisotropy at D″. Faster *SH* velocity is observed beneath the circum-Pacific region [e.g., *Lay and Helmberger*, 1983; *Lay and Young*, 1991; *Kendall and Silver*, 1996; *Ritsema*, 2000], while mixed anisotropy ($V_{SH} > V_{SV}$ or $V_{SH} < V_{SV}$) is reported in the LLSVP beneath the South Pacific [e.g., *Kendall and Silver*, 1996; *Pulliam and Sen*, 1998; *Ritsema et al*., 1998; *Russell et al*., 1998; *Vinnik et al*., 1998; *Fouch et al*., 2001; *Ford et al*., 2006]. There are some disagreements between these findings and the D″ features observed in the whole-mantle anisotropic models shown in Figure 8. First, SAW642ANb does not show faster *SH* velocity beneath circum-Pacific regions, especially for Alaska and Siberia, while other models do. Second, all anisotropic models show faster *SV* velocity to some extent in the LLSVP beneath the South Pacific, inconsistent with regional studies. As shown below in section 5, isotropic structure can leak into D″ anisotropic structure in these global inversions, which is partly responsible for the faster *SV* velocity in the whole-mantle anisotropic models. As explained in section 2.4, we adopted stronger damping for the anisotropic structure to suppress this leakage, which may be the reason for the weaker amplitudes of the faster *SV* velocity in the two LLSVPs in SGLOBE-rani compared with the other models. S362WMANI + M and SAVANI show stronger anomalies in the lower mantle (up to 2%) than other models.

SGLOBE-rani shows some features not seen in previous whole-mantle models, such as narrow linear anomalies with faster *SV* velocity along subduction zones in the transition zone (at ~400–660 km). Considering the slip system [001](010) for a water content of 50–230 wt ppm H_2O of Wadsleyite [*Kawazoe et al*., 2013], the faster *SV* velocity that we observe at upper transition zone depths may be caused by horizontal shear due to stagnant subducting slabs. It is also notable that a strong faster *SH* velocity is observed beneath the Fiji-Tonga region from the transition zone to ~1400 km depth, which may result from midmantle interaction between a strong upwelling and the Tonga slab. Our resolution tests (section 5) suggest that these features are robust.

Cross sections of Voigt isotropy and radial anisotropy perturbations across the Pacific and Africa are presented in Figure 11. A subducting slab (high-velocity anomaly) is observed from the Japan Trench in Figure 11a, which is stagnant beneath Asia. Faster *SH* velocity is observed in the asthenosphere beneath the Pacific (Figure 11c) as we discussed before, but this feature is close to the reference value near the East

Pacific Rise. The thickness of the faster *SH* velocity region increases with distance from the East Pacific Rise, possibly partly consistent with a half-space cooling model with seafloor age. However, the thickness of this layer decreases when approaching the Japan Trench.

In Figure 11b, two subducting slabs are shown beneath the Aegean Sea and Scotia Sea, albeit with some smearing effects. In the cross section of Figure 11d, it is noteworthy that subducting slabs beneath the Aegean Sea and Scotia Sea are associated with faster *SV* velocities in the upper mantle. This kind of relationship is also observed beneath the Pacific slab subducted beneath the Japan Trench in Figure 11c. This may be related to the dipping angle of subducting slabs [*Chang et al*., 2010; *Song and Kawakatsu*, 2012], since oceanic asthenosphere with faster *SH* velocity of radial anisotropy may generate faster *SV* velocity of radial anisotropy when subducting steeply. Another interesting feature regarding subducting slabs is that in some cases they may induce faster *SH* velocity of radial anisotropy in the lower mantle just beneath them, as seen beneath the Japan Trench and the Aegean Sea, where the subducting slabs reach to the transition zone. Since the viscosity of the lower mantle is much higher than that in the upper mantle, the shear stress associated with the penetrating or stagnant slabs may lead to intense deformation in the subslab lower mantle, generating seismic anisotropy with faster *SH* velocity [*Faccenda*, 2014]. This observation may help constrain the characteristics of viscosity, composition, and flow of materials in the lower mantle.

4.3. Power Spectra and Correlations of Whole-Mantle Models

Figure 12 shows the power spectra of various whole-mantle models for perturbations in V_{Voigt} isotropy and radial anisotropy (ξ) as a function of depth and angular order, up to degree 35. Compared with the other models, our isotropic SGLOBE-rani model shows a widespread power spectrum over all angular orders up to degree 35 in the whole mantle, showing that it has smaller-scale heterogeneity than other models. However, it shows the strongest power mostly concentrated in the upper mantle, similar to SAVANI, while S362WMANI + M and SAW642ANb have strong power down to the uppermost lower mantle. As found in previous studies [e.g., *Kustowski et al*., 2008], all models show high degree-two power in the D″, corresponding to the two LLSVPs and slab graveyards observed in this region (Figure 6).

As for the power spectra of perturbations in radial anisotropy ξ (Figure 12b), SAVANI shows the widest spread power over almost all angular orders in the whole mantle, indicating that it has stronger and smaller-scale anomalies in radial anisotropy than the other models. Nevertheless, its strongest power spectrum is confined to the upper mantle, similar to the SGLOBE-rani and SAW642ANb models, while S362WMANI + M shows a strong power spectrum persistent down to the lower mantle.

Correlations between SGLOBE-rani and other global models for spherical harmonic expansions up lmax = 12, 20, and 35 are presented in Figure 13. The V_{Voigt} correlation between SGLOBE-rani and S40RTS is excellent, exceeding 0.6 in the whole mantle, even for lmax = 35. Likewise, the correlation with SAVANI is also high (Figure 13a), possibly because SGLOBE-rani and SAVANI are constructed using, among other data sets, some of the data used to build the S40RTS model. In the upper mantle, the correlation between SGLOBE-rani and GAP_P4 is the worst, but still ~0.6, confirming the strong correlation between upper mantle isotropic structure in the various models. In some cases the correlation decreases with increasing depth, notably around ~1300 km depth for the SAW64ANb model. In the D″, the correlations are high, being about 0.6 or larger for all the models.

As expected, the radial anisotropy ξ model correlations (Figure 13b) are worse than for V_{Voigt} (Figure 13a). The ξ correlation between SLOBE-rani and SAVANI is the best, being around 0.5 in the whole mantle. However, the ξ correlations between SGLOBE-rani and the other models are quite low, consistent with results from previous studies, notably by *Kustowski et al.* [2008], where correlations lower than 0.3 were found between degree-8 expansions of the models SAW64ANb and S362WMANI. Hence, the ξ correlations between SGLOBE-rani and the recent SAVANI model of around 0.5 are actually encouraging, especially given that different regularization schemes were used in the construction of these models, with SAVANI using a distinct depth-dependent damping scheme for the anisotropic structure.

4.4. Crustal Thickness Perturbations

Figure 14 shows the crustal thickness perturbations from CRUST2.0 obtained in our inversions along with CRUST2.0 and the perturbations added to CRUST2.0. We observe thicker crustal thickness along the

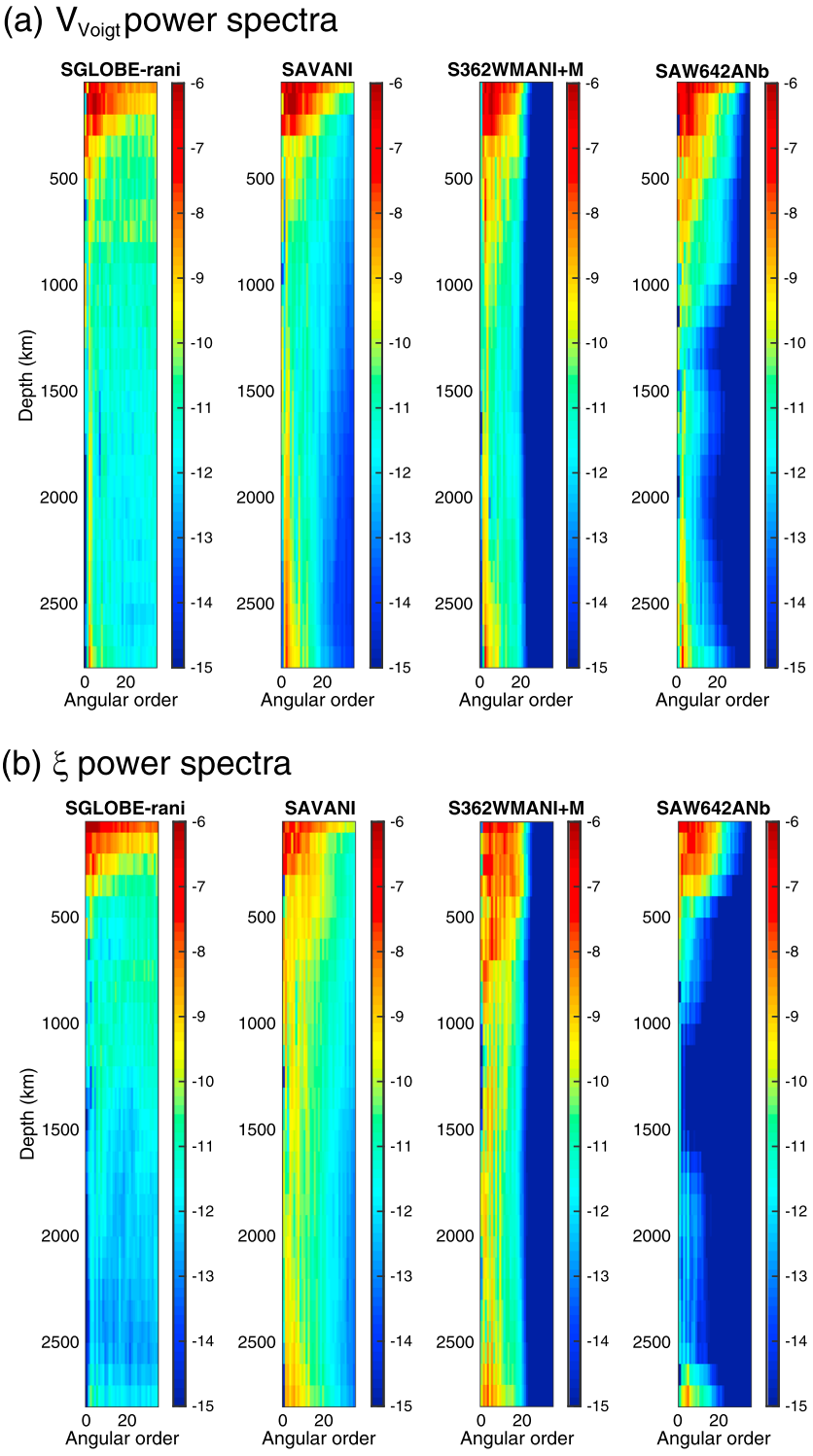

Figure 12. Power spectra of various global models plotted using a logarithmic color scale as a function of depth and angular order up to degree 35 for (a) V_{Voigt} isotropic structure perturbations and (b) variations in radial anisotropy (ξ).

subduction zones in the western Pacific, possibly due to the superposition of two oceanic crusts. The thickest crustal thickness perturbations are observed beneath the Ontong Java Plateau in the Pacific, which was formed by a massive magmatic eruption possibly by a mantle plume [e.g., *Tarduno et al.*, 1991], thereby resulting in thicker crust than nearby oceanic crusts. These observations suggest that our model of

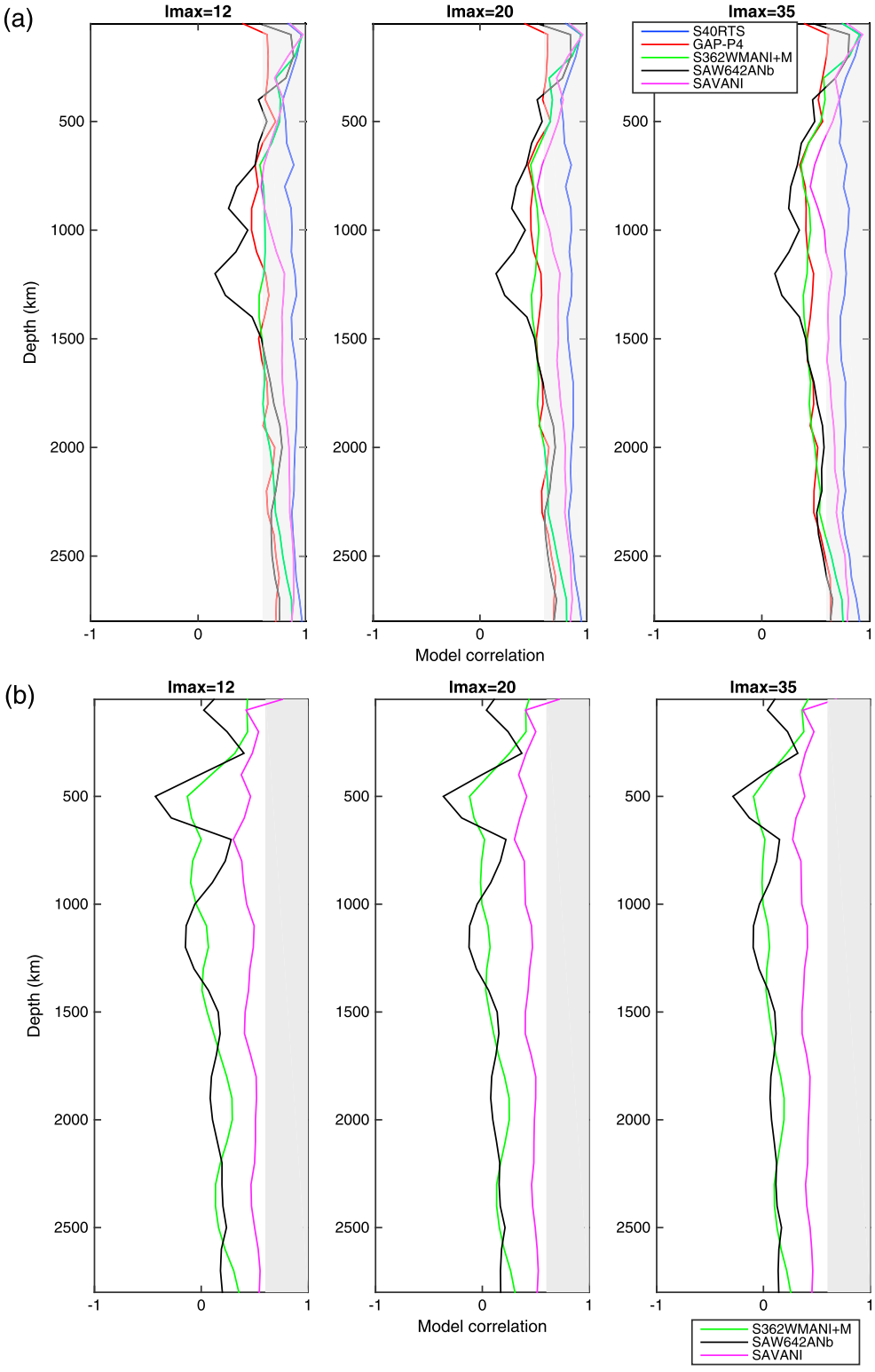

Figure 13. (a) V_{Voigt} and (b) ξ correlations between SGLOBE-rani and other global models as a function of depth for spherical harmonic expansions of the models up to lmax = 12, 20, and 35. The shaded region corresponds to correlation coefficients larger than 0.6.

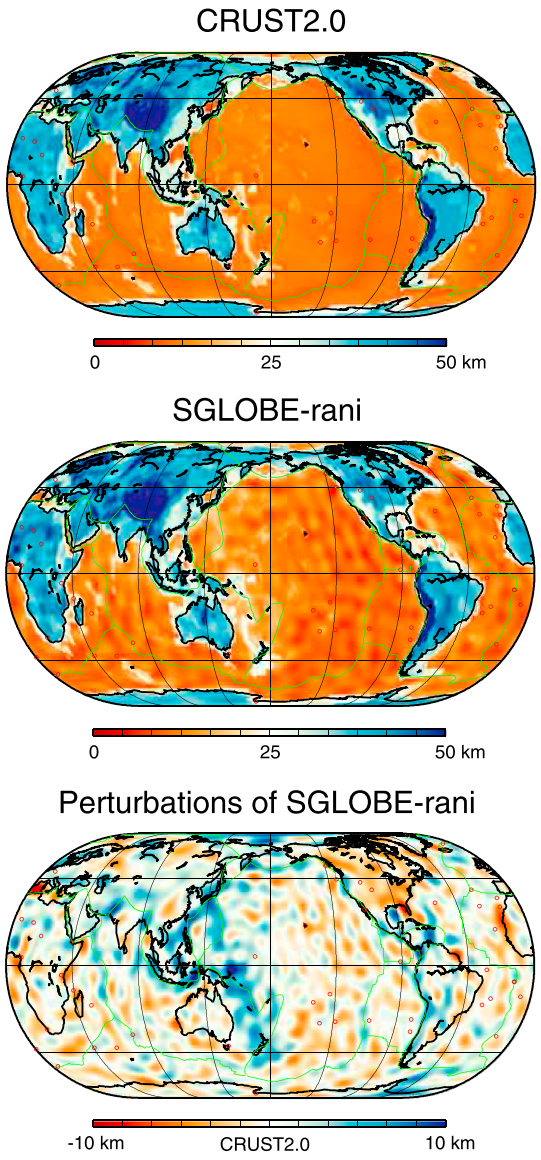

Figure 14. Crustal maps from (a) CRUST2.0, (b) SGLOBE-rani, and (c) crustal thickness perturbations of SGLOBE-rani from CRUST2.0.

crustal thickness perturbations may contain some valuable information about the crust, especially beneath oceans, which remain more challenging to access than continental crust.

Since we only invert for crustal thickness perturbations, and not for crustal velocity perturbations, the retrieved crustal thickness variations may be contaminated by uncorrected crustal velocity information. For example, the thinner crust obtained beneath the cratons of North America may be due to relatively high crustal velocity. On the other hand, the relatively thicker crustal thickness obtained beneath Tibet and Pamir may be due to low crustal velocity reported in the region [e.g., *Owens and Zandt*, 1997]. Therefore, we need to compare our results with those from other crustal studies, such as receiver function analyses, to identify more clearly which features of SGLOBE-rani reflect real crustal thickness perturbations. This will be the subject of a future study.

5. Resolution Tests

To illustrate the resolving power of the data sets and the robustness of our tomographic models, we present the results from three resolution tests. First, we carried out checkerboard tests. Figure 15 demonstrates the excellent resolution for Voigt average isotropic structure of 1000 km wide checkers with 5% perturbations. In the lower mantle, there is some horizontal smearing, but the signs of the anomalies are well recovered without much interference. As expected, the resolution for the anisotropic structure (Figure 16) is worse than that for isotropy because of weaker sensitivity of the data to anisotropy (about half). However, there is quite good resolution for the upper mantle and transition zone, except for the South Pacific and Africa, where the data coverage is poorer. Resolution in the lower mantle is poor, but there is still fair resolution in regions below the Pacific's rim, Eurasia, and North America in the lower mantle and the whole D″ region.

Second, we performed resolution tests for crustal thickness perturbations (Figure 17). We set perturbations from CRUST2.0 with respect to the Moho depth in PREM as the true model. The output model loses some small-scale features by smoothing them due to the parameterization used, but it is encouraging to see that large perturbations of about 30 km can be well resolved beneath Tibet and Andes, despite the use of 1-D sensitivity kernels for crustal thickness perturbations.

Third, we test the leakage from isotropic to anisotropic structure, similar to the tests carried out by *Chang et al.* [2014] and by *Kustowski et al.* [2008], but now for a much larger data set. The input model corresponds to the isotropic structure in SGLOBE-rani (shown in Figure 6) and the radially anisotropic structure in PREM (i.e., only 1-D variations from the Moho down to 220 km depth). Figure 18 shows the output anisotropic model obtained, where some conspicuous anomalies are observed at 100 and 2800 km depths with a similar pattern to the input isotropic anomalies. This suggests the leakage from isotropic to

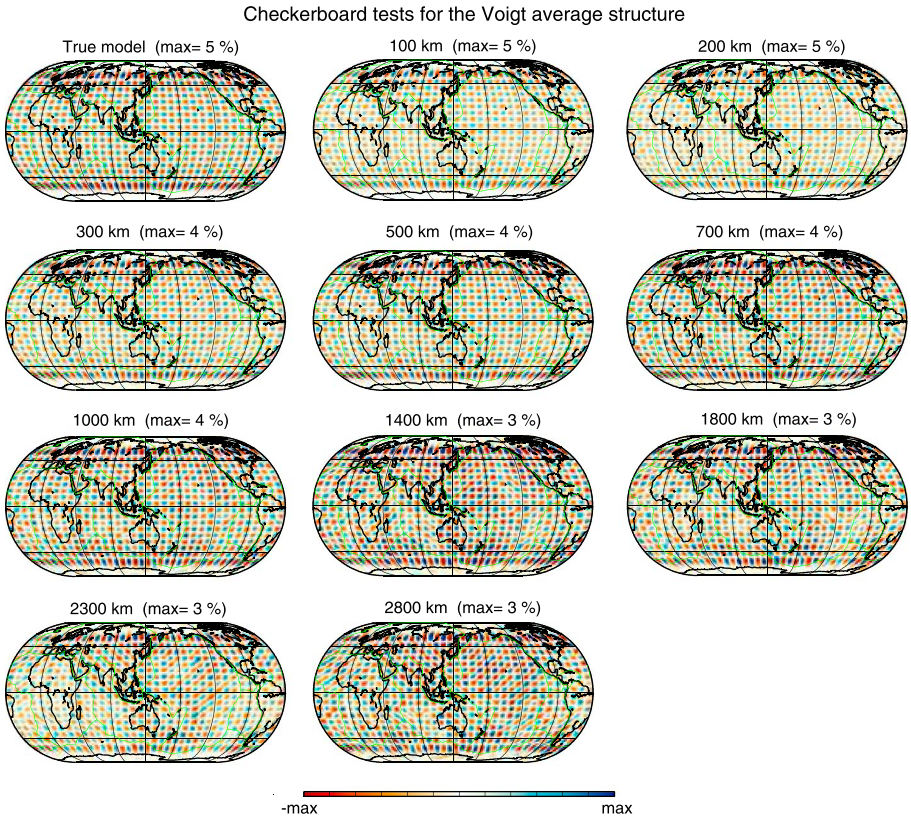

Figure 15. Checkerboard tests for the isotropic structure retrieved in our inversions with the data sets used in the construction of SGLOBE-rani. The true model is shown on the top left side, and output depth slices are shown for 100, 200, 300, 500, 700, 1000, 1400, 1800, 2300, and 2800 km depths. The range of model amplitude variations is shown at the top of each depth slice.

anisotropic imaged structure. The negative anisotropic anomaly (i.e., $V_{SV} > V_{SH}$) at 100 km may result from the positive isotropic V_S anomaly beneath cratons, while the negative anisotropic anomaly at 2800 km results from negative isotropic anomaly in Large Low Shear Velocity Provinces (LLSVPs) at the bottom of the Earth's mantle. By comparison with the inversion results of surface wave data only, we found that the leakage at shallow and deep mantle are caused by the body wave travel time data. This is due to the fact that body waves traverse quasi-vertically in the shallow mantle and quasi-horizontally at the bottom of the mantle, which leads to an unbalanced sensitivity to V_{SV} and V_{SH} in these regions. High-velocity anomalies in cratons result in shorter travel times, which are mapped as high-velocity isotropic anomalies or faster *SV* velocity of radial anisotropy, since the negative anisotropy reduces travel times where quasi-vertical incidence is dominant. In contrast, low isotropic velocity anomalies in LLSVPs lead to longer travel times, which can be leaked into faster *SV* velocity of radial anisotropy, since quasi-horizontal paths are dominant here. Compared with the anisotropic model that we obtained from real data inversions in Figure 8, the perturbations at 100 km in the output test model have opposite signs, so this leakage at the shallowest depth will lead to an underestimation of the amplitude of the anomalies at 100 km depth. However, the anomalies at 2800 km depth have the same sign as the retrieved anisotropic model from real data inversions (Figure 8), which indicates that at least some portion of the observed faster *SV* velocity anisotropy within LLSVPs may be leaked from the isotropic structure [e.g., *Panning and Romanowicz*, 2004].

6. Data Misfit Analysis

We further assess the robustness of the radial anisotropy structure in SGLOBE-rani by comparing inversions for crustal thickness perturbations, isotropic and radially anisotropic structures with separate inversions for

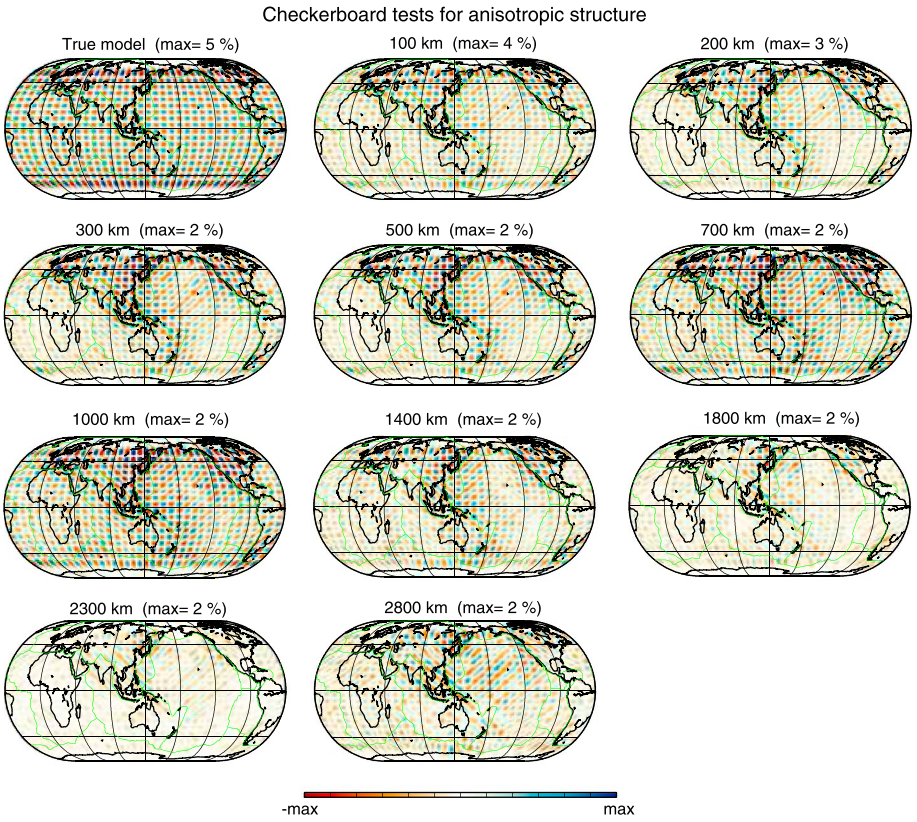

Figure 16. Same as in Figure 15 but for radially anisotropic structure.

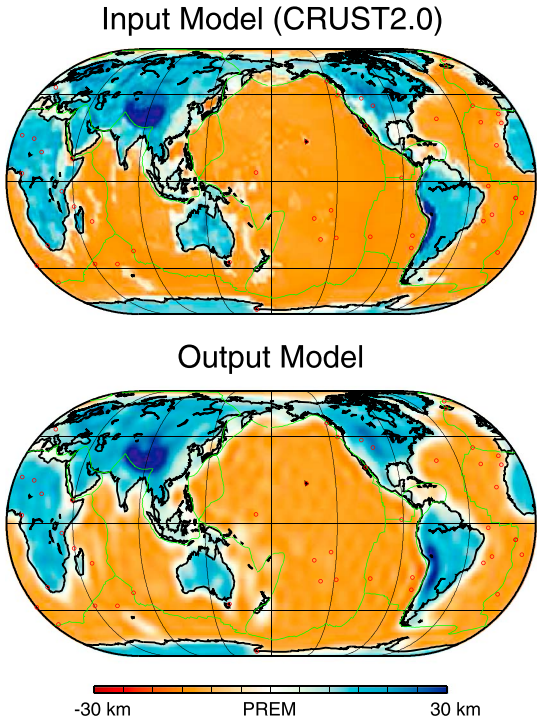

Figure 17. Resolution test for crustal thickness perturbations. CRUST2.0 is used as the input model, and the resulting output model from the test is at the bottom.

isotropic structure alone. Figure 19 shows data misfit curves for body and surface waves obtained from our joint inversions for v_S, ζ_S, and d, where the data misfit is depicted as a function of the effective number of parameters. The data misfit m^2 is calculated as

$$m^2 = \frac{(Ax - d)^T (Ax - d)}{d^T d}, \tag{8}$$

where **x** is the solution model expressed as perturbations from the starting model, A is the kernel matrix, and **d** is the data vector (differences to predictions for the starting model). The effective number of parameters is given by the trace of the resolution matrix. As the effective number of parameters increases, the data misfits decrease (Figure 19). Beyond 17,000 free parameters, the data misfits reduce more slowly. Hence, in this study we show and analyze the model with 17,000 free parameters.

When comparing models obtained from different inversions (e.g., for radially anisotropic and isotropic structures versus isotropic-only structure), it is essential to ensure that the models have the exact same number of free parameters

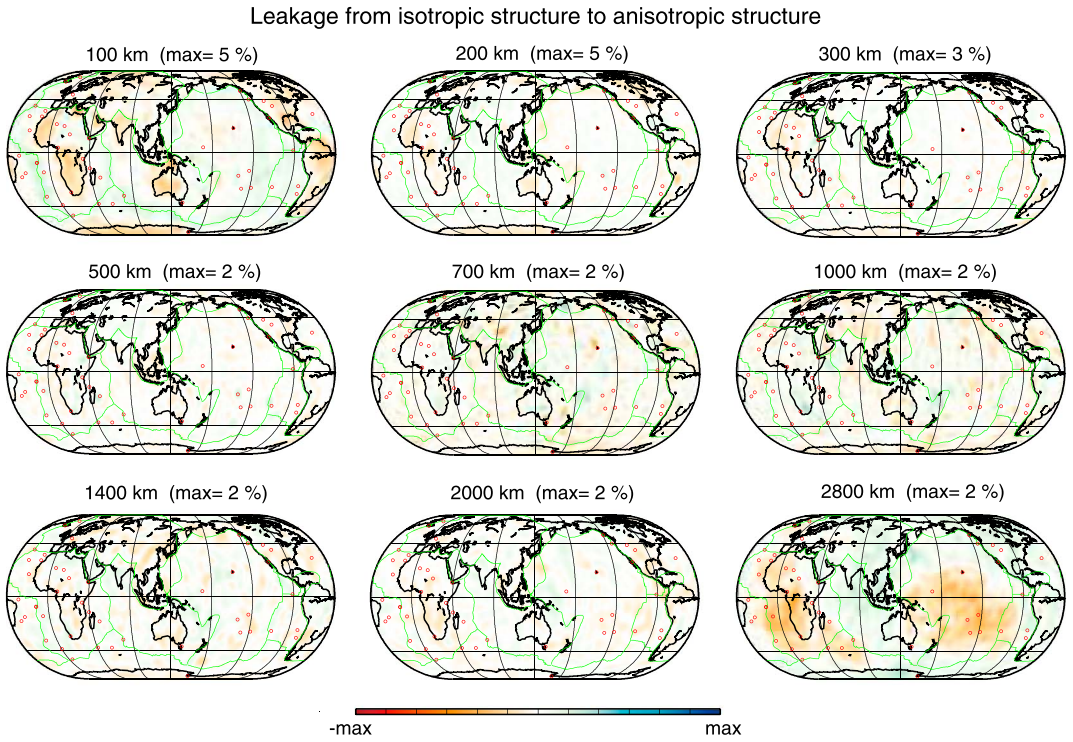

Figure 18. Output of synthetic test to investigate trade-offs between isotropic and radially anisotropic structures in the mantle (see main text for details). Depth slices of leakage from the isotropic model of SGLOBE-rani to anisotropic structure are shown for 100, 200, 300, 500, 700, 1000, 1400, 2000, and 2800 km depths. The range of model amplitude variations is shown at the top of each depth slice.

for rigorous comparisons. Overall, we obtain a variance reduction of ~8% for surface wave data when adopting lateral variations of radial anisotropy and of crustal thickness in our inversions (Table 3) for models with 17,000 free parameters. Table 3 shows that from an isotropic inversion (i.e., not allowing perturbations in radial anisotropy from PREM), we obtain an overall misfit value of 0.329. If we include lateral variations in radial anisotropy, we acquire a misfit value of 0.274, resulting in a variance reduction of ~5.5% compared to the isotropic inversion. Finally, if we also include crustal thickness perturbations as model parameters, we gain a further misfit reduction of ~2.9%, with a misfit value of 0.245, thereby obtaining an overall 8.4% misfit reduction compared with the isotropic inversion. This is a substantial variance reduction, especially when compared with *Ferreira et al.*'s [2010] report that allowing lateral variations of radial anisotropy in the inversions resulted in a variance reduction of only ~1–2%, which is similar to the effect of using different crust models for crustal corrections. Therefore, this result indicates that it is possible to constrain 3-D radial anisotropy beyond the error range due to crustal effects.

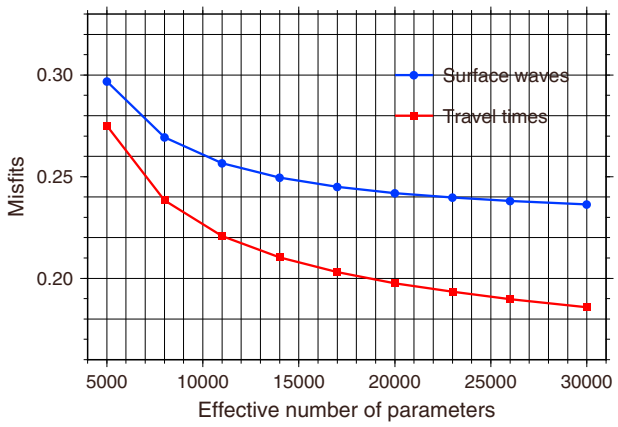

Figure 19. Surface wave and body wave data misfit values (equation (8)) as a function of the effective number of model parameters from joint inversions for isotropic and radially anisotropic structures and crustal thickness perturbations.

However, the misfit values of body wave travel time data hardly changed in all cases, which indicates that our body

Table 3. Overall L_2-Norm Data Misfit Values[a]

	Surface Wave Misfit	Travel Time Misfit
1. Isotropic inversion	0.329	0.202
2. +Radial anisotropy	0.274	0.204
3. +Crustal thickness	0.245	0.203

[a]The misfit values are with respect to the initial misfits (equation (8)); m^2 =1 for the starting model) for surface wave and body wave travel time data from inversions for (1) isotropic structure only (i.e., not allowing lateral variations in radial anisotropy), (2) isotropic and radially anisotropic structure, and (3) isotropic and radially anisotropic structures and crustal thickness perturbations. All the models have a total of 17,000 effective number of parameters.

wave data set does not necessarily require radial anisotropy at the bottom of the mantle and that isotropic structure can be easily leaked into anisotropic structure when using travel time data only, as shown in Figure 18. Therefore, we have to be cautious when interpreting anisotropic results for depths where rays are travelling quasivertically or quasi-horizontally and with poor surface wave sensitivity.

7. Conclusions

We construct a new radially anisotropic *S* velocity model, SGLOBE-rani, using a wide range of surface wave phase-velocity, group-velocity, and teleseismic body wave travel time data. In total, we incorporated ~43,000,000 surface wave measurements and ~420,000 body wave travel time data.

Our *S* velocity isotropic model is consistent with the large-scale features in previous whole-mantle isotropic models, and it also shares many similarities with upper mantle models SL2013sv [*Schaeffer and Lebedev*, 2013] and SEMum2 [*French et al*., 2013], such as low-velocity anomalies at 100 km depth beneath Tibet and Mongolia and linear features associated with subducting slabs in the transition zone. Moreover, our isotropic *S* velocity images seem to have many similarities to the high-resolution *P* velocity model GAP_P4 when imaging the structure of subducted slabs in the transition zone.

Qualitatively, our radially anisotropic model seems to agree better with results from regional studies than other previous whole-mantle anisotropic models. However, similar to previous work by *Kustowski et al.* [2008] and *Chang et al.* [2014], we find a substantial mapping of isotropic structure into D″ anisotropic structure, notably beneath the two LLSVPs beneath the Pacific and Africa. This suggests that there is still much scope for improvement in the robust global imaging of D″ anisotropy. Nevertheless, our new model of 3-D radial anisotropy shows some features not seen in previous whole-mantle models, such as narrow linear anomalies with faster *SV* velocity along subduction zones in the transition zone and faster *SH* velocity beneath slabs in the lower mantle. Finally, crustal thickness perturbations in SGLOBE-rani show thicker crustal thickness along subduction zones, which may be due to the superposition of two oceanic crusts at trenches.

Acknowledgments

We thank Masayuki Obayashi in JAMSTEC, who kindly provided cross sections from his models. This research was initially supported by the Leverhulme Trust (project F/00 204/AS), followed by support by NERC project NE/K005669/1 and by the Korea Meteorological Administration Research and Development Program under grant CATER-2014-8030. This study was also supported by 2013 Research Grant from Kangwon National University. It was carried out initially on the High Performance Computing Cluster supported by the Research and Specialist Computing Support services at the University of East Anglia followed by the national UK supercomputing facilities HECToR and Archer. Chris Collins is particularly thanked for his outstanding support regarding our HPC needs. A.M.G.F. also thanks funding by the European Commission's Initial Training Network project QUEST (contract FP7- PEOPLE-ITN-2008-238007; www.quest-itn.org). We gratefully acknowledge the availability of global seismograms from the IRIS/IDA/USGS, GEOSCOPE, and GEOFON networks and the IRIS Data Center.

References

Aki, K., and K. Kaminuma (1963), Phase velocity of Love waves in Japan (part 1): Love waves from the Aleutian shock of March 1957, *Bull. Earthquake Res. Inst.*, *41*, 243–259.

Anderson, D. L. (1961), Elastic wave propagation in layered anisotropic media, *J. Geophys. Res.*, *66*, 2953–2963, doi:10.1029/JZ066i009p02953.

Anderson, D. L. (1965), Recent evidence concerning the structure and composition of the Earth's mantle, *Phys. Chem. Earth*, *6*, 1–131.

Anderson, O. L., E. Schreiber, R. C. Liebermann, and N. Soga (1968), Some elastic constant data on minerals relevant to geophysics, *Rev. Geophys.*, *6*, 491–524, doi:10.1029/RG006i004p00491.

Auer, L., L. Boschi, T. W. Becker, T. Nissen-Meyer, and D. Giardini (2014), Savani: A variable resolution whole-mantle model of anisotropic shear velocity variations based on multiple data sets, *J. Geophys. Res. Solid Earth*, *119*, 3006–3034, doi:10.1002/2013JB010773.

Bassin, C., G. Laske, and G. Masters (2000), The current limits of resolution for surface wave tomography in North America, *Eos Trans. AGU*, *81*, Abstract S12A-03.

Beghein, C., and J. Trampert (2003), Probability density functions for radial anisotropy: Implications for the upper 1200 km of the mantle, *Earth Planet. Sci. Lett.*, *217*, 151–162.

Beghein, C., and J. Trampert (2004), Probability density functions for radial anisotropy from fundamental mode surface wave data and the Neighbourhood Algorithm, *Geophys. J. Int.*, *157*, 1163–1174.

Beghein, C., J. Trampert, and H. J. van Heijst (2006), Radial anisotropy in seismic reference models of the mantle, *J. Geophys. Res.*, *111*, B02303, doi:10.1029/2005JB003728.

Bozdağ, E., and J. Trampert (2008), On crustal corrections in surface wave tomography, *Geophys. J. Int.*, *172*, 1066–1082.

Cara, M., and J. J. Lévêque (1988), Anisotropy of the asthenosphere: The higher mode data of the Pacific revisited, *Geophys. Res. Lett.*, *15*, 205–208, doi:10.1029/GL015i003p00205.

Chang, S.-J., and S. van der Lee (2011), Mantle plumes and associated flow beneath Arabia and East Africa, *Earth Planet. Sci. Lett.*, *302*, 448–454.

Chang, S.-J., S. van der Lee, E. Matzel, and H. Bedle (2010), Radial anisotropy along the Tethyan margin, *Geophys. J. Int.*, *182*, 1013–1024.

Chang, S.-J., A. M. G. Ferreira, J. Ritsema, H. J. van Heijst, and J. H. Woodhouse (2014), Global radially anisotropic mantle structure from multiple datasets: A review, current challenges, and outlook, *Tectonophysics*, *617*, 1–19.

Debayle, E., and B. L. N. Kennett (2000), Anisotropy in the Australian upper mantle from Love and Rayleigh waveform inversion, *Earth Planet. Sci. Lett.*, *184*, 339–351.
Debayle, E., J.-J. Lévêque, and M. Cara (2001), Seismic evidence for a deeply rooted low-velocity anomaly in the upper mantle beneath the northeastern Afro/Arabian continent, *Earth Planet. Sci. Lett.*, *193*, 423–436.
Dziewoński, A. M., and D. L. Anderson (1981), Preliminary reference Earth model, *Phys. Earth Planet. Inter.*, *25*, 297–356.
Ekström, G. (2011), A global model of Love and Rayleigh surface wave dispersion and anisotropy, 25-250 s, *Geophys. J. Int.*, *187*, 1668–1686.
Ekström, G., and A. M. Dziewoński (1998), The unique anisotropy of the Pacific upper mantle, *Nature*, *394*, 168–172.
Ekström, G., J. Tromp, and E. W. F. Larson (1997), Measurements and global models of surface wave propagation, *J. Geophys. Res.*, *102*, 8137–8157, doi:10.1029/96JB03729.
Faccenda, M. (2014), Mid mantle seismic anisotropy around subduction zones, *Phys. Earth Planet. Inter.*, *227*, 1–19.
Ferreira, A. M. G., J. H. Woodhouse, K. Visser, and J. Trampert (2010), On the robustness of global radially anisotropic surface wave tomography, *J. Geophys. Res.*, *115*, B04313, doi:10.1029/2009JB006716.
Ford, S., E. J. Garnero, and A. K. McNamara (2006), A strong lateral shear velocity gradient and anisotropy heterogeneity in the lowermost mantle beneath the southern Pacific, *J. Geophys. Res.*, *111*, B03306, doi:10.1029/2004JB003574.
Fouch, M. J., K. M. Fischer, and M. Wysession (2001), Lowermost mantle anisotropy beneath the Pacific: Imaging the ousrce of the Hawaiian plume, *Earth Planet. Sci. Lett.*, *190*, 167–180.
French, S., V. Lekic, and B. Romanowicz (2013), Waveform tomography reveals channeled flow at the base of the oceanic asthenosphere, *Science*, *342*, 227–230.
Fukao, Y., and M. Obayashi (2013), Subducted slabs stagnant above, penetrating through, and trapped below the 660 km discontinuity, *J. Geophys. Res. Solid Earth*, *118*, 5920–5938, doi:10.1002/2013JB010466.
Gu, Y. J., A. L. Lerner-Lam, A. M. Dziewoński, and G. Ekström (2005), Deep structure and seismic anisotropy beneath the East Pacific Rise, *Earth Planet. Sci. Lett.*, *232*, 259–272.
Gung, Y., M. Panning, and B. Romanowicz (2003), Global anisotropy and the thickness of continents, *Nature*, *422*, 707–711.
Hansen, S., A. A. Nyblade, and M. Benoit (2012), Mantle structure beneath Africa and Arabia from adaptively parameterized *P wave* tomography: Implications for the origin of Cenozoic Afro-Arabian tectonism, *Earth Planet. Sci. Lett.*, *319–320*, 23–34.
Hess, R. (1964), Seismic anisotropy of the uppermost mantle under the oceans, *Nature*, *203*, 629–631.
Ishii, M., and J. Tromp (1999), Normal-mode and free-air gravity constraints on lateral variations in velocity and density of Earth's mantle, *Science*, *285*, 1231–1236.
Jung, H., and S.-I. Karato (2001), Water-induced fabric transitions in olivine, *Science*, *293*, 1460–1463.
Karato, S.-I., H. Jung, I. Katayama, and P. Skemer (2008), Geodynamic significance of seismic anisotropy of the upper mantle: New insights from laboratory studies, *Annu. Rev. Earth Planet. Sci.*, *36*, 59–95.
Kawazoe, T., T. Ohuchi, Y. Nishihara, N. Nishiyama, K. Fujino, and T. Irifune (2013), Seismic anisotropy in the mantle transition zone induced by shear deformation of wadsleyite, *Phys. Earth Planet. Inter.*, *216*, 91–98.
Kendall, J.-M., and P. G. Silver (1996), Constraints from seismic anisotropy on the nature of the lowermost mantle, *Nature*, *381*, 409–412.
Kustowski, B., A. M. Dziewoński, and G. Ekström (2007), Nonlinear crustal corrections for normal-mode seismograms, *Bull. Seismol. Soc. Am.*, *97*, 1756–1762.
Kustowski, B., G. Ekström, and A. M. Dziewoński (2008), Anisotropic shear-wave velocity structure of the Earth's mantle: A global model, *J. Geophys. Res.*, *113*, B06306, doi:10.1029/2007JB005169.
Lay, T., and D. Helmberger (1983), The shear-wave velocity-gradient at the base of the mantle, *J. Geophys. Res.*, *88*, 8160–8170, doi:10.1029/JB088iB10p08160.
Lay, T., and C. Young (1991), Analysis of seismic *SV* waves in the core's penumbra, *Geophys. Res. Lett.*, *18*, 1373–1376, doi:10.1029/91GL01691.
Lebedev, S., J. M.-C. Adam, and T. Meier (2013), Mapping the Moho with seismic surface waves: A review, resolution analysis, and recommended inversion strategies, *Tectonophysics*, *609*, 377–394, doi:10.1016/j.tecto.2012.12.030.
Lekić, V., and B. Romanowicz (2011), Inferring upper-mantle structure by full waveform tomography with the spectral element method, *Geophys. J. Int.*, *185*, 799–831.
Lekić, V., M. Panning, and B. Romanowicz (2010), A simple method for improving crustal corrections in waveform tomography, *Geophys. J. Int.*, *182*, 265–278.
Lévêque, J.-J., and M. Cara (1985), Inversion of multimode surface wave data: Evidence for sub-lithospheric anisotropy, *Geophys. J. R. Astron. Soc.*, *83*, 753–773.
Love, A. E. H. (1927), *A Treatise on the Theory of Elasticity*, Cambridge Univ. Press, Cambridge, U. K.
Marone, F., and B. Romanowicz (2007), Non-linear crustal corrections in high-resolution regional waveform seismic tomography, *Geophys. J. Int.*, *170*, 460–467.
McEvilly, T. V. (1964), Central U.S. crust-upper mantle structure from Love and Rayleigh wave phase velocity inversion, *Bull. Seismol. Soc. Am.*, *54*, 1997–2015.
Montagner, J.-P. (1998), Where can seismic anisotropy be detected in the Earth's mantle? In boundary layers, *Pure Appl. Geophys.*, *151*, 223–256.
Montagner, J.-P., and D. L. Anderson (1989), Constrained reference mantle model, *Phys. Earth Planet. Inter.*, *58*, 205–227.
Montagner, J.-P., and B. L. N. Kennett (1996), How to reconcile body-wave and normal-mode reference Earth models, *Geophys. J. Int.*, *125*, 229–248.
Montagner, J.-P., and T. Tanimoto (1991), Global upper mantle tomography of seismic velocities and anisotropies, *J. Geophys. Res.*, *96*, 20,337–20,351, doi:10.1029/91JB01890.
Mooney, W. D., G. Laske, and G. Masters (1998), CRUST5.1: A global crustal model at 5° × 5°, *J. Geophys. Res.*, *103*, 727–747, doi:10.1029/97JB02122.
Moulik, P., and G. Ekström (2014), An anisotropic shear velocity model of the Earth's mantle using normal modes, body waves, surface waves and long-period waveforms, *Geophys. J. Int.*, *199*, 1713–1738.
Nataf, H.-C., I. Nakanishi, and D. L. Anderson (1984), Anisotropy and shear-velocity heterogeneities in the upper mantle, *Geophys. Res. Lett.*, *11*, 109–112, doi:10.1029/GL011i002p00109.
Nataf, H.-C., I. Nakanishi, and D. L. Anderson (1986), Measurements of mantle wave velocities and inversion for lateral heterogeneities and anisotropy 3. Inversion, *J. Geophys. Res.*, *91*, 7261–7307, doi:10.1029/JB091iB07p07261.
Nettles, M., and A. M. Dziewoński (2008), Radially anisotropic shear velocity structure of the upper mantle globally and beneath North America, *J. Geophys. Res.*, *113*, B02303, doi:10.1029/2006JB004819.
Nishimura, C. E., and D. W. Forsyth (1989), The anisotropic structure of the upper mantle in the Pacific, *Geophys. J. Int.*, *96*, 203–229.
Nyblade, A. A. (2011), The upper-mantle low-velocity anomaly beneath Ethiopia, Kenya, and Tanzania: Constraints on the origin of the African superswell in eastern Africa and plate versus plume models of mantle dynamics, *Geol. Soc. Am. Spec. Pap.*, *478*, 37–50.

Owens, T. J., and G. Zandt (1997), Implications of crustal property variations for models of Tibetan plateau evolution, *Nature*, *387*, 37–43.
Panning, M., and B. Romanowicz (2004), Inferences on flow at the base of the Earth's mantle based on seismic anisotropy, *Science*, *303*, 351–353.
Panning, M., and B. Romanowicz (2006), A three-dimensional radially anisotropic model of shear velocity in the whole mantle, *Geophys. J. Int.*, *167*, 361–379.
Panning, M. P., V. Lekić, and B. Romanowicz (2010), Importance of crustal corrections in the development of a new global model of radial anisotropy, *J. Geophys. Res.*, *115*, B12325, doi:10.1029/2010JB007520.
Pulliam, J., and M. K. Sen (1998), Seismic anisotropy in the core-mantle transition zone, *Geophys. J. Int.*, *135*, 113–128.
Resovsky, J., and J. Trampert (2003), Using probabilistic seismic tomography to test mantle velocity-density relationships, *Earth Planet. Sci. Lett.*, *215*, 121–134.
Ritsema, J. (2000), Evidence for shear velocity anisotropy in the lowermost mantle beneath the Indian Ocean, *Geophys. Res. Lett.*, *27*, 1041–1044, doi:10.1029/1999GL011037.
Ritsema, J., T. Lay, E. J. Garnero, and H. Benz (1998), Seismic anisotropy in the lowermost mantle beneath the Pacific, *Geophys. Res. Lett.*, *25*, 1229–1232, doi:10.1029/98GL00913.
Ritsema, J., H. J. van Heijst, and J. H. Woodhouse (2004), Global transition zone tomography, *J. Geophys. Res.*, *109*, B02302, doi:10.1029/2003JB002610.
Ritsema, J., H. J. van Heijst, J. H. Woodhouse, and A. Deuss (2009), Long-period body wave traveltimes through the crust: Implication for crustal corrections and seismic tomography, *Geophys. J. Int.*, *179*, 1255–1261.
Ritsema, J., A. Deuss, H. J. van Heijst, and J. H. Woodhouse (2011), S40RTS: A degree-40 shear-velocity model for the mantle from new Rayleigh wave dispersion, teleseismic traveltime and normal-mode splitting function measurements, *Geophys. J. Int.*, *184*, 1223–1236.
Ritzwoller, M. H., and A. L. Levshin (1998), Eurasian surface wave tomography: Group velocities, *J. Geophys. Res.*, *103*, 4839–4878, doi:10.1029/97JB02622.
Robertson, G. S., and J. H. Woodhouse (1995), Evidence for proportionality of *P* and *S* heterogeneity in the lower mantle, *Geophys. J. Int.*, *123*, 85–116.
Rodi, W. L., P. Glover, T. M. C. Li, and S. S. Alexander (1975), A fast, accurate method for computing group-velocity partial derivatives for Rayleigh and Love modes, *Bull. Seismol. Soc. Am.*, *65*, 1105–1114.
Russell, S. A., T. Lay, and E. J. Garnero (1998), Seismic evidence for small-scale dynamics in the lowermost mantle at the root of the Hawaiian hotspot, *Nature*, *396*, 255–258.
Schaeffer, A. J., and S. Lebedev (2013), Global shear speed structure of the upper mantle and transition zone, *Geophys. J. Int.*, *194*, 417–449.
Shapiro, N. M., and M. H. Ritzwoller (2002), Monte-Carlo inversion for a global shear-velocity model of the crust and upper mantle, *Geophys. J. Int.*, *151*, 88–105.
Silver, P. G. (1996), Seismic anisotropy beneath the continents: Probing the depths of geology, *Annu. Rev. Earth Planet. Sci.*, *24*, 385–432.
Song, T.-R. A., and H. Kawakatsu (2012), Subduction of oceanic asthenosphere: Evidence from sub-slab seismic anisotropy, *Geophys. Res. Lett.*, *39*, L17301, doi:10.1029/2012GL052639.
Takeo, A., K. Nishida, T. Isse, H. Kawakatsu, H. Shiobara, H. Sugioka, and T. Kanazawa (2013), Radially anisotropic structure beneath the Shikoku Basin from broadband surface wave analysis of ocean bottom seismometer records, *J. Geophys. Res. Solid Earth*, *118*, 2878–2892, doi:10.1002/jgrb.50219.
Takeuchi, H., and M. Saito (1972), Seismic surface waves, in *Methods of Computational Physics*, vol. 11, edited by B. A. Bolt, pp. 217–295, Academic Press, New York.
Tarduno, J. A., W. V. Sliter, L. Kroenke, M. Leckie, H. Mayer, J. J. Mahoney, R. Musgrave, M. Storey, and E. L. Winterer (1991), Rapid formation of Ontong Java Plateau by Aptian mantle plume volcanism, *Science*, *254*, 399–403.
van Heijst, H. J., and J. Woodhouse (1999), Global high-resolution phase velocity distributions of overtone and fundamental-mode surface waves determined by mode branch stripping, *Geophys. J. Int.*, *137*, 601–620.
Vinnik, L. P., L. Breger, and B. Romanowicz (1998), Anisotropic structures at the base of the Earth's mantle, *Nature*, *393*, 564–567.
Visser, K., J. Trampert, S. Lebedev, and B. L. N. Kennett (2008), Probability of radial anisotropy in the deep mantle, *Earth Planet. Sci. Lett.*, *270*, 241–250.
Woodhouse, J. H. (1981), A note on the calculation of travel times in a transversely isotropic Earth model, *Phys. Earth Planet. Inter.*, *25*, 357–359.
Woodhouse, J. H., and F. A. Dahlen (1978), The effect of a general aspherical perturbation on the free oscillations of the Earth, *Geophys. J. R. Astron. Soc.*, *53*, 335–354.
Woodhouse, J. H., and T. P. Girnius (1982), The calculation of $d\Delta/dp$ and of partial derivatives for travel-time inversion in transversely isotropic spherical Earth models, in *Seismic Discrimination, Semiannual Technical Summary Report to the Defense Advanced Research Projects Agency*, pp. 61–65, MIT, Lincoln Lab., Lexington, Mass.